HAL
open science

An improved explicit scheme for whole-building hygrothermal simulation

Suelen Gasparin, Julien Berger, Denys Dutykh, Nathan Mendes

To cite this version:

Suelen Gasparin, Julien Berger, Denys Dutykh, Nathan Mendes. An improved explicit scheme for whole-building hygrothermal simulation. 2017. hal-01495737v1

HAL Id: hal-01495737
https://hal.science/hal-01495737v1

Preprint submitted on 26 Mar 2017 (v1), last revised 17 Apr 2018 (v2)

HAL is a multi-disciplinary open access archive for the deposit and dissemination of scientific research documents, whether they are published or not. The documents may come from teaching and research institutions in France or abroad, or from public or private research centers.

L'archive ouverte pluridisciplinaire **HAL**, est destinée au dépôt et à la diffusion de documents scientifiques de niveau recherche, publiés ou non, émanant des établissements d'enseignement et de recherche français ou étrangers, des laboratoires publics ou privés.

Distributed under a Creative Commons Attribution - NonCommercial - ShareAlike 4.0 International License

Suelen Gasparin
Pontifical Catholic University of Paraná, Brazil

Julien Berger
Pontifical Catholic University of Paraná, Brazil

Denys Dutykh
CNRS, Université Savoie Mont Blanc, France

Nathan Mendes
Pontifical Catholic University of Paraná, Brazil

An improved explicit scheme for whole-building hygrothermal simulation

arXiv.org / HAL

Last modified: March 26, 2017

An improved explicit scheme for whole-building hygrothermal simulation

Suelen Gasparin*, Julien Berger, Denys Dutykh, and Nathan Mendes

Abstract. Although implicit methods require extra calculation, they have been largely used for obtaining numerical approximations of time-dependent differential conservation equations in the building science domain, thanks to their stability conditions that enable the use of larger time steps. Nevertheless, they require important sub-iterations when dealing with highly nonlinear problems such as the combined heat and moisture transfer through porous building elements or when the whole-building is simulated and there is important coupling among the building elements themselves and among neighbouring zones and HVAC systems. On the other hand, the classical explicit Euler scheme is generally not used because its stability condition imposes very fine time discretisation. Hence, this paper explores the use of an improved explicit approach - the Dufort–Frankel scheme - to overcome the disadvantage of the classical explicit one and to bring benefits that cannot be obtained by implicit methods. The Dufort–Frankel approach is first compared to the classical implicit and explicit Euler schemes to compute the solution of both linear and nonlinear heat and moisture transfer through porous materials. Then, the analysis of the Dufort–Frankel unconditionally stable explicit scheme is extended to the coupled heat and moisture balances on the scale of a one- and a two-zone building models. The Dufort–Frankel scheme has the benefits of being unconditionally stable, second-order accurate in time $\mathcal{O}(\Delta t^2)$ and to compute explicitly the solution at each time step, avoiding costly sub-iterations. This approach may reduce the computational cost by twenty as well as it may enable perfect synchronism for whole-building simulation and co-simulation. In addition, it can be easier parallelised on high-performance computer systems.

Key words and phrases: heat and moisture transfer; numerical methods; finite differences; explicit schemes; Dufort–Frankel scheme; whole-building simulation

MSC: [2010] 35R30 (primary), 35K05, 80A20, 65M32 (secondary)

PACS: [2010] 44.05.+e (primary), 44.10.+i, 02.60.Cb, 02.70.Bf (secondary)

Key words and phrases. heat and moisture transfer; numerical methods; finite differences; explicit schemes; Dufort–Frankel scheme; whole-building simulation.

* Corresponding author.

Contents

1 Introduction **4**

2 Porous building element hygrothermal model **5**

3 Numerical schemes **8**

3.1 The Euler explicit scheme 9

3.2 The Euler implicit scheme 10

3.3 Improved explicit scheme: Dufort–Frankel method 10

3.4 Validation of the numerical solution 12

4 Numerical application **12**

4.1 Linear case 13

4.2 Nonlinear case 14

5 Whole-building hygrothermal model **18**

5.1 Coupling the lumped air multizone model with the transfer through porous walls . . . 18

5.2 Implicit scheme for the whole-building energy simulation: problem statement 22

5.3 Improved explicit schemes for the whole-building energy simulations 24

6 Numerical application **24**

6.1 Linear case 25

6.2 Nonlinear case 26

7 Conclusion **31**

A The Dufort–Frankel scheme for weakly coupled equations **36**

B Dimensionless numerical values **38**

B.1 Wall model with linear material properties 38

B.2 Whole-building model with linear material properties 38

References **42**

1. Introduction

Models for the combined heat and moisture transfer through porous building elements have been implemented in building simulation tools since the 1990's in software such as Delphin [2], MATCH [25], MOIST [5], WUFI [11] and UMIDUS [9, 19, 21] among others. More recently, those models have been implemented in whole-building simulation tools and tested in the frame of the International Energy Agency Annex 41, which reported on most of detailed models and their successful applications for accurate assessment of hygrothermal transfer in buildings [31].

The Euler and Crank–Nicolson implicit schemes have been used in many studies and implemented in building simulation tools, as reported in the literature [2, 11, 15, 16, 18, 20, 26, 27, 30], due to their numerical property of unconditional stability. Nevertheless, at every time step, one has to use a tridiagonal solver to invert the linear system of equations to determine the solution value at the following time layer. For instance in [20], a multi-tridiagonal matrix algorithm has been developed to compute the solution of coupled equations of nonlinear heat and moisture transfer, using an Euler implicit scheme. Furthermore, when dealing with nonlinearities, as when material properties are moisture content or temperature dependent, one has to perform *sub-iterations* to linearise the system, increasing the total CPU time. In [15], thousands of sub-iterations are reported to converge to the solution of a mass diffusion problem. Another disadvantage of implicit schemes appears when coupling the wall model, representing the transfer phenomena in porous building elements, to the room air model. The wall and the room air models must iterate within one time step until reaching a given tolerance [14]. If it does not impose any limitation on the choice of the time discretisation, it induces sub-iterations that increase the computational time of the simulation of the whole-building model. Moreover, it is valuable to decrease this computational cost knowing that the hygrothermal and energy building simulation is generally carried out for time scale periods as long as one year, or even more. However, the phenomena and particularly the boundary conditions evolve a time scale of seconds.

Recently, in [12], the improved explicit Dufort–Frankel scheme was explored for the solution of moisture diffusion equation highlighting that the standard stability limitation can be overcome, which inspired to investigate the use of the Dufort–Frankel scheme for the solution of the combined heat and moisture transfer through porous building elements coupled with room air models.

In this way, this paper first describes in Section 2 the heat and moisture transfer model. In Section 3, basics of the Dufort–Frankel explicit scheme is detailed before exploring the features of the scheme applied to linear and nonlinear cases, presented in Section 4. Then, the benefits of using an unconditionally stable explicit scheme are investigated to perform a whole-building hygrothermal simulation based on coupling the porous element model to a room air multizone model.

2. Porous building element hygrothermal model

The physical problem considers one-dimensional heat and moisture transfer through a porous material defined by the spatial domain $\Omega_x = [0, L]$. The following convention is adopted: $x = 0$ corresponds to the surface in contact with the inside room and, $x = L$, corresponds to the outside surface. The moisture transfer occurs due to capillary migration and vapour diffusion. The heat transfer is governed by diffusion and latent mechanisms. The physical problem can be formulated as [15, 28]:

$$\frac{\partial \rho_w}{\partial t} = \frac{\partial}{\partial x}\left(k_l \frac{\partial P_c}{\partial x} + \delta_v \frac{\partial P_v}{\partial x} \right), \tag{2.1a}$$

$$\left(\rho_0 c_0 + \rho_w c_w\right) \frac{\partial T}{\partial t} + c_w T \frac{\partial \rho_w}{\partial t} = \frac{\partial}{\partial x}\left(\lambda \frac{\partial T}{\partial x} + L_v \delta_v \frac{\partial P_v}{\partial x} \right), \tag{2.1b}$$

where ρ_w is the volumetric moisture content of the material, δ_v and k_l, the vapour and liquid permeabilities, P_v, the vapour pressure, T, the temperature, R_v, the water vapour gas constant, P_c the capillary pressure, c_0, the material heat capacity, ρ_0, the material density, c_w the water heat capacity, λ the thermal conductivity, and, L_v the latent heat of evaporation. Eq. (2.1a) can be written using the vapour pressure P_v as the driving potential. For this, we consider the physical relation, known as the Kelvin equation, between P_v and P_c, and the Clausius–Clapeyron equation:

$$P_c = \rho_l R_v T \ln\left(\frac{P_v}{P_s(T)}\right),$$
$$\frac{\partial P_c}{\partial P_v} = \frac{R_v T}{P_v}.$$

Neglecting the variation of the capillary pressure and the mass content with temperature [26], the partial derivative of P_c can be written as:

$$\frac{\partial P_c}{\partial x} = \frac{\partial P_c}{\partial P_v}\frac{\partial P_v}{\partial x} + \frac{\partial P_c}{\partial T}\frac{\partial T}{\partial x} \simeq \frac{R_v T}{P_v}\frac{\partial P_v}{\partial x}.$$

In addition, we have:

$$\frac{\partial \rho_w}{\partial t} = \frac{\partial \rho_w}{\partial \phi}\frac{\partial \phi}{\partial P_v}\frac{\partial P_v}{\partial t} + \frac{\partial \rho_w}{\partial T}\frac{\partial T}{\partial t} \simeq \frac{\partial \rho_w}{\partial \phi}\frac{\partial \phi}{\partial P_v}.$$

Considering the relation $\rho_w = \mathrm{f}(\phi)$, obtained from material properties, and from the relation between the vapour pressure P_v and the relative humidity ϕ, we get:

$$\frac{\partial \rho_w}{\partial t} = \frac{\mathrm{f}'(\phi)}{P_s}\frac{\partial P_v}{\partial t}.$$

We denote by

$k_M \overset{\text{def}}{:=} k_l \dfrac{R_v T}{P_v} + \delta_v$ the total moisture transfer coefficient under vapour pressure gradient ,

$k_{TM} \overset{\text{def}}{:=} L_v \, \delta_v$ the heat coefficient due to a vapour pressure gradient ,

$k_{TT} \overset{\text{def}}{:=} \lambda$ the heat transfer coefficient under temperature gradient ,

$c_M \overset{\text{def}}{:=} \dfrac{\mathrm{f}'(\phi)}{P_s(T)}$ the moisture storage coeficient ,

$c_{TT} \overset{\text{def}}{:=} \rho_0 \, c_0 + \mathrm{f}(\phi) \, c_w$ the energy storage coeficient ,

$c_{TM} \overset{\text{def}}{:=} c_w \, T$ the coupling storage coefficient .

Considering the previous notation, Eq. (2.1) can be rewritten as:

$$c_M \frac{\partial P_v}{\partial t} = \frac{\partial}{\partial x}\left(k_M \frac{\partial P_v}{\partial x} \right), \tag{2.2a}$$

$$c_{TT} \frac{\partial T}{\partial t} + c_{TM} \frac{\partial P_v}{\partial t} = \frac{\partial}{\partial x}\left(k_{TT} \frac{\partial T}{\partial x} + k_{TM} \frac{\partial P_v}{\partial x} \right) \tag{2.2b}$$

The boundary conditions at the interface between the porous material and the air are expressed as:

$$k_M \frac{\partial P_v}{\partial x} = h_M \left(P_v - P_{v,\infty} \right) - g_\infty , \tag{2.3a}$$

$$k_{TT} \frac{\partial T}{\partial x} + k_{TM} \frac{\partial P_v}{\partial x} = h_T \left(T - T_\infty \right) + L_v \, h_M \left(P_v - P_{v,\infty} \right) - q_\infty , \tag{2.3b}$$

where $P_{v,\infty}$ and T_∞ stand for the vapour pressure and temperature of the air and h_M and h_T are the convective transfer coefficients. If the bounding surface is in contact with the outside building air, g_∞ is the liquid flux from wind driven rain and q_∞ is the total heat flux from radiation and the heat contribution from the inward liquid water penetration. If the bounding surface is in contact with the inside building air, $g_\infty = 0$ and q_∞ is the distributed short-wave radiative heat transfer rate q_{rw} in the enclosure and long-wave radiative heat exchanged among the room surfaces:

$$q_{\mathrm{rw}} = \sum_{w=1}^{m} \mathrm{s} \, \epsilon \, \sigma \left(\left(T_w(\, x = 0 \,) \right)^4 - \left(T(\, x = 0 \,) \right)^4 \right),$$

where s is the view factor between two surfaces, σ is the Stefan–Boltzmann constant, ϵ is the emissivity of the wall surface, w represents the m bounding walls. We consider a uniform vapour pressure and temperature distributions as initial conditions:

$$P_v = P_{v,i} , \qquad t = 0 , \tag{2.4a}$$

$$T = T_i , \qquad t = 0 . \tag{2.4b}$$

The governing equations can be written in a dimensionless form as:

$$c_M^\star \frac{\partial v}{\partial t^\star} = \mathrm{Fo}_M \frac{\partial}{\partial x^\star}\left(k_M^\star \frac{\partial v}{\partial x^\star} \right), \tag{2.5a}$$

$$c_{TT}^\star \frac{\partial u}{\partial t^\star} + c_{TM}^\star \gamma \frac{\partial v}{\partial t^\star} = \mathrm{Fo}_{TT} \frac{\partial}{\partial x^\star}\left(k_{TT}^\star \frac{\partial u}{\partial x^\star} \right) + \mathrm{Fo}_{TM}\, \gamma \frac{\partial}{\partial x^\star}\left(k_{TM}^\star \frac{\partial v}{\partial x^\star}. \right) \tag{2.5b}$$

and the boundary condition as:

$$k_M^\star \frac{\partial v}{\partial x^\star} = \mathrm{Bi}_M \left(v - v_\infty \right) - g_\infty^\star, \tag{2.6a}$$

$$\mathrm{Fo}_{TT}\, k_{TT}^\star \frac{\partial u}{\partial x^\star} + k_{TM}^\star \mathrm{Fo}_{TM} \gamma \frac{\partial v}{\partial x^\star} = \mathrm{Bi}_{TT} \left(u - u_\infty \right) + \mathrm{Bi}_{TM} \left(v - v_\infty \right) - q_\infty^\star, \tag{2.6b}$$

where the dimensionless quantities are defined as:

$$u \overset{\text{def}}{:=} \frac{T}{T_i}, \quad v \overset{\text{def}}{:=} \frac{P_v}{P_{v,i}}, \quad u_\infty \overset{\text{def}}{:=} \frac{T_\infty}{T_i}, \quad v_\infty \overset{\text{def}}{:=} \frac{P_{v,\infty}}{P_{v,i}},$$

$$x^\star \overset{\text{def}}{:=} \frac{x}{L}, \quad t^\star \overset{\text{def}}{:=} \frac{t}{t_0}, \quad c_M^\star \overset{\text{def}}{:=} \frac{c_M}{c_{M,0}}, \quad c_{TT}^\star \overset{\text{def}}{:=} \frac{c_{TT}}{c_{TT,0}},$$

$$c_{TM}^\star \overset{\text{def}}{:=} \frac{c_{TM}}{c_{TM,0}}, \quad k_M^\star \overset{\text{def}}{:=} \frac{k_M}{k_{M,0}}, \quad k_{TT}^\star \overset{\text{def}}{:=} \frac{k_{TT}}{k_{TT,0}}, \quad k_{TM}^\star \overset{\text{def}}{:=} \frac{k_{TM}}{k_{TM,0}},$$

$$\mathrm{Fo}_M \overset{\text{def}}{:=} \frac{t_0 \cdot k_{M,0}}{L \cdot c_{M,0}}, \quad \mathrm{Fo}_{TT} \overset{\text{def}}{:=} \frac{t_0 \cdot k_{TT,0}}{L \cdot c_{TT,0}}, \quad \mathrm{Fo}_{TM} \overset{\text{def}}{:=} \frac{t_0 \cdot k_{TM,0}}{L \cdot c_{TM,0}}, \quad \gamma \overset{\text{def}}{:=} \frac{c_{TM,0} \cdot P_{v,i}}{c_{TT,0} \cdot T_i},$$

$$\mathrm{Bi}_M \overset{\text{def}}{:=} \frac{h_M \cdot L}{k_{M,0}}, \quad \mathrm{Bi}_{TT} \overset{\text{def}}{:=} \frac{h_T \cdot L}{k_{TT,0}}, \quad \mathrm{Bi}_{TM} \overset{\text{def}}{:=} \frac{L_v \cdot h_M \cdot L \cdot P_{v,i}}{k_{TT,0} \cdot T_i}, \quad g_\infty^\star \overset{\text{def}}{:=} \frac{L}{P_{v,i} \cdot k_{M,0}} g_\infty,$$

$$q_\infty^\star \overset{\text{def}}{:=} \frac{L}{T_i \cdot k_{TT,0}} q_\infty.$$

The dimensionless formulation enables to determine important scaling parameters (Biot and Fourier numbers for instance). Henceforth, solving one dimensionless problem is equivalent to solve a whole class of dimensional problems sharing the same scaling parameters. Then, dimensionless equations allow to estimate the relative magnitude of various terms, and thus, eventually to simplify the problem using asymptotic methods [22]. Finally, the floating point arithmetics is designed such as the rounding errors are minimal if you manipulate the numbers of the same magnitude [17]. Moreover, the floating point numbers have the highest density in the interval $(0, 1)$ and their density decays exponentially when we move further away from zero. So, it is always better to manipulate numerically the quantities at the order of $\mathcal{O}(1)$ to avoid severe round-off errors and to likely improve the conditioning of the problem in hands.

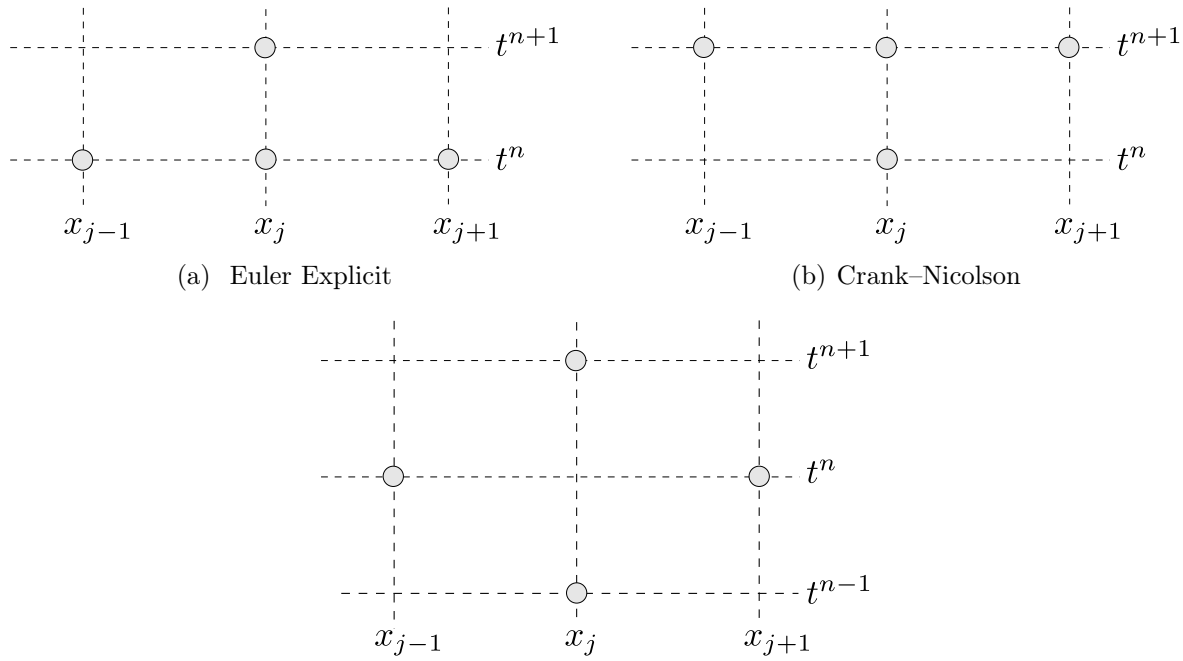

(a) Euler Explicit (b) Crank–Nicolson

(c) Dufort–Frankel

Figure 1. *Stencils of the numerical schemes.*

3. Numerical schemes

Let us consider a uniform discretisation of the interval $\Omega_x \rightsquigarrow \Omega_{L_x}$:

$$\Omega_h = \bigcup_{j=0}^{N-1} [x_j, x_{j+1}], \qquad x_{j+1} - x_j \equiv \Delta x, \quad \forall j \in \{0, 1, \ldots, N-1\}.$$

The time layers are uniformly spaced as well $t^n = n\Delta t$, $\Delta t = \text{const} > 0$, $n = 0, 1, 2, \ldots, N_t$ The values of the function $u(x, t)$ in discrete nodes will be denoted by $u_j^n \stackrel{\text{def}}{:=} u(x_j, t^n)$.

For the sake of simplicity and without loosing generality, simple diffusion equation is considered:

$$\frac{\partial u}{\partial t} = \nabla \cdot (\nu \nabla u). \tag{3.1}$$

First, the numerical schemes are explained considering the linear case. Then, the extension to the nonlinear case is described.

3.1. The Euler explicit scheme

The standard explicit EULER scheme can be written as:

$$\frac{u_j^{n+1} - u_j^n}{\Delta t} = \nu \frac{u_{j-1}^n - 2\,u_j^n + u_{j+1}^n}{\Delta x^2}, \qquad j = 1, \dots, N-1, \qquad n \geqslant 0. \tag{3.2}$$

The stencil of this scheme is shown in Figure 1(a). The discretisation is completed using the two boundary conditions:

$$\begin{aligned} u_0^n &= \psi_{\mathrm{L}}\,(t^n, u_1^n, \dots), \\ u_N^n &= \psi_{\mathrm{R}}\,(t^n, u_{N-1}^n, \dots), \end{aligned}$$

where functions $\psi_{\mathrm{L,R}}\,(\bullet)$ may depend on adjacent values of the solution whose number depends on the approximation order of the scheme (here we use the second order in space).

By solving Eq. (3.2) with respect to u_j^{n+1}, we obtain a discrete dynamical system

$$u_j^{n+1} = u_j^n + \nu \frac{\Delta t}{\Delta x^2}\left(u_{j-1}^n - 2\,u_j^n + u_{j+1}^n\right), \qquad n \geqslant 0,$$

whose starting value is directly obtained from the initial condition:

$$u_j^0 = 1.$$

It is well-known that scheme (3.2) approximates the continuous operator to order $\mathcal{O}(\Delta t + \Delta x^2)$. The explicit scheme is conditionally stable under the following COURANT–FRIEDRICHS–LEWY (CFL) condition:

$$\Delta t \leqslant \frac{1}{2\,\nu}\,\Delta x^2. \tag{3.3}$$

Unfortunately, this condition is too restrictive for sufficiently fine discretisations so that this approach is hardly used in building simulation tools. In the case of linear weakly coupled equations, as Eq. (2.5), the CFL condition is calculated as the more restrictive one.

For the nonlinear case, the EULER scheme yields to:

$$\frac{u_j^{n+1} - u_j^n}{\Delta t} = \frac{1}{\Delta x}\left[\left(\nu\,\frac{\partial u}{\partial x}\right)^n_{j+\frac{1}{2}} - \left(\nu\,\frac{\partial u}{\partial x}\right)^n_{j-\frac{1}{2}}\right], \tag{3.4}$$

with

$$\left(\nu\frac{\partial u}{\partial x}\right)^n_{j+\frac{1}{2}} = \frac{1}{2\,\Delta x}\,\nu^n_{j+\frac{1}{2}}\left(u_{j+1}^n - u_j^n\right).$$

3.2. The Euler implicit scheme

In order to overcome the stability condition Eq. (3.3), the EULER implicit scheme can be used, written as:

$$\frac{u_j^{n+1} - u_j^n}{\Delta t} = \nu \frac{u_{j-1}^{n+1} - 2\,u_j^{n+1} + u_{j+1}^{n+1}}{\Delta x^2}, \qquad j = 1, \ldots, N-1, \qquad n \geqslant 0. \tag{3.5}$$

The finite-difference stencil of this scheme is depicted in Figure 1(b). These relations have to be properly initialized and supplemented with numerical boundary conditions. The scheme (3.5) has the same order of accuracy as the explicit scheme (3.2), *i.e.* $\mathcal{O}(\Delta t + \Delta x^2)$. However, the implicit scheme (3.5) is unconditionally stable, which constitutes its major advantage.

The most important difference with the explicit scheme (3.2) is that a tridiagonal system of linear algebraic equations to determine the numerical solution values $\{u_j^{n+1}\}_{j=0}^N$ on the following time layer $t = t^{n+1}$ has to be solved, which determines the algorithm complexity. A tridiagonal system of equations are solved in $\mathcal{O}(N)$ operations (using the simple THOMAS algorithm, for example) at every iteration step.

The straightforward application of the scheme for the nonlinear case yields the following scheme:

$$\frac{u_j^{n+1} - u_j^n}{\Delta t} = \frac{1}{\Delta x}\left[\left(\nu \frac{\partial u}{\partial x}\right)_{j+\frac{1}{2}}^{n+1} - \left(\nu \frac{\partial u}{\partial x}\right)_{j-\frac{1}{2}}^{n+1}\right], \tag{3.6}$$

with

$$\left(\nu \frac{\partial u}{\partial x}\right)_{j+\frac{1}{2}}^{n+1} = \frac{1}{2\,\Delta x}\,\nu_{j+\frac{1}{2}}^{n+1}\left(u_{j+1}^{n+1} - u_j^{n+1}\right).$$

However, this approach inevitably leads to deal with nonlinearities due to the evaluation of thermal properties at the upcoming time layer $t = t^{n+1}$. To deal with this issue, local linearisation techniques such as fixed-point or local linearisation strategies [6, 23] can be used, requiring a relatively high number of sub-iterations.

3.3. Improved explicit scheme: Dufort–Frankel method

Using the so-called DUFORT–FRANKEL method, the numerical scheme is expressed as:

$$\frac{u_j^{n+1} - u_j^{n-1}}{2\,\Delta t} = \nu \frac{u_{j-1}^n - \left(u_j^{n-1} + u_j^{n+1}\right) + u_{j+1}^n}{\Delta x^2}, \qquad j = 1, \ldots, N-1, \quad n \geqslant 1, \tag{3.7}$$

where the term $2\,u_j^n$ is replaced by $u_j^{n-1} + u_j^{n+1}$. The scheme (3.7) has the stencil depicted in Figure 1(c). At a first glance, the scheme (3.7) looks like an implicit scheme, however, it

is not truly the case. Eq. (3.7) can be easily solved for u_j^{n+1} to give the following discrete dynamical system:

$$u_j^{n+1} = \frac{1 - \lambda}{1 + \lambda} u_j^{n-1} + \frac{\lambda}{1 + \lambda} \left(u_{j+1}^n + u_{j-1}^n \right), \qquad n \geqslant 1,$$

where:

$$\lambda \overset{\text{def}}{:=} 2\,\nu \frac{\Delta t}{\Delta x^2}.$$

The standard VON NEUMANN stability analysis shows that the DUFORT–FRANKEL scheme is *unconditionally stable* [12, 24, 29]. The consistency error analysis of the scheme (3.7) shows the following result:

$$\mathcal{L}_j^n = \nu \frac{\Delta t^2}{\Delta x^2} \frac{\partial^2 u}{\partial t^2} + \frac{\partial u}{\partial t} - \nu \frac{\partial^2 u}{\partial x^2} + \frac{1}{6} \Delta t^2 \frac{\partial^3 u}{\partial t^3} - \frac{1}{12} \nu \Delta x^2 \frac{\partial^4 u}{\partial x^4} - \frac{1}{12} \nu \Delta t^2 \Delta x \frac{\partial^5 u}{\partial x^3 \partial t^2} + \mathcal{O}\left(\frac{\Delta t^4}{\Delta x^2} \right), \quad (3.8)$$

where

$$\mathcal{L}_j^n \overset{\text{def}}{:=} \frac{u_j^{n+1} - u_j^{n-1}}{2\,\Delta t} - \nu \frac{u_{j-1}^n - \left(u_j^{n-1} + u_j^{n+1} \right) + u_{j+1}^n}{\Delta x^2}.$$

So, from the asymptotic expansion for $\mathcal{L}_j^n$ one can see the DUFORT–FRANKEL scheme is second-order accurate in time and:

- First-order accurate in space if $\Delta t \propto \Delta x^{3/2}$
- Second-order accurate in space if $\Delta t \propto \Delta x^2$.

In the nonlinear case, the numerical scheme can be derived as follows:

$$\frac{u_j^{n+1} - u_j^{n-1}}{2\,\Delta t} = \frac{1}{\Delta x} \left[\left(\nu \frac{\partial u}{\partial x} \right)_{j+\frac{1}{2}}^n - \left(\nu \frac{\partial u}{\partial x} \right)_{j-\frac{1}{2}}^n \right]. \quad (3.9)$$

The right-hand side term can be expressed as:

$$\frac{1}{\Delta x} \left(\left(\nu \frac{\partial u}{\partial x} \right)_{j+\frac{1}{2}}^n - \left(\nu \frac{\partial u}{\partial x} \right)_{j-\frac{1}{2}}^n \right) = \frac{1}{\Delta x^2} \left(\nu_{j+\frac{1}{2}}^n u_{j+1}^n - \nu_{j-\frac{1}{2}}^n u_{j-1}^n - \left(\nu_{j+\frac{1}{2}}^n - \nu_{j-\frac{1}{2}}^n \right) u_j^n \right). \quad (3.10)$$

Using the DUFORT–FRANKEL stencil (see Figure 1(c)), the term u_j^n is replaced by $\frac{u_j^{n+1} + u_j^{n-1}}{2}$. Thus, considering Eq. (3.9), the DUFORT–FRANKEL schemes can be expressed as an explicit scheme:

$$u_j^{n+1} = \frac{\lambda_1}{\lambda_0 + \lambda_3} \cdot u_{j+1}^n + \frac{\lambda_2}{\lambda_0 + \lambda_3} \cdot u_{j-1}^n + \frac{\lambda_0 - \lambda_3}{\lambda_0 + \lambda_3} \cdot u_j^{n-1}, \qquad n \geqslant 1,$$

with

$$\lambda_0 \stackrel{\text{def}}{:=} 1\,, \qquad \lambda_1 \stackrel{\text{def}}{:=} \frac{2\,\Delta t}{\Delta x^2}\,\nu^n_{j+\frac{1}{2}}\,,$$

$$\lambda_2 \stackrel{\text{def}}{:=} \frac{2\,\Delta t}{\Delta x^2}\,\nu^n_{j-\frac{1}{2}}\,, \qquad \lambda_3 \stackrel{\text{def}}{:=} \frac{\Delta t}{\Delta x^2}\left(\nu^n_{j+\frac{1}{2}} + \nu^n_{j-\frac{1}{2}}\right).$$

When dealing with the nonlinearities of the material properties, an interesting feature of explicit schemes is that it does not require any sub-iterations (using NEWTON–RAPHSON approach for instance). At the time layer n, the material properties $\nu_{j+\frac{1}{2}}$, $\nu_{j-\frac{1}{2}}$ are *explicitly* calculated at t^n. It should be noted that the material properties evaluated at $j + \frac{1}{2}$ is formulated as:

$$\nu^n_{j+\frac{1}{2}} = \nu\left(\frac{u^n_j + u^n_{j+1}}{2}\right).$$

3.4. Validation of the numerical solution

One possible comparison of the numerical schemes can be done by computing the $\mathcal{L}_\infty$ error between the solution u_{num} and a reference solution u_{ref}:

$$\varepsilon \stackrel{\text{def}}{:=} \left|\left| u_{\text{ref}} - u_{\text{num}} \right|\right|_\infty$$

The reference solution is computed using the `Matlab` open source package `Chebfun` [10]. Using the function `pde23t`, it enables to compute a numerical solution of a partial derivative equation using the CHEBYSHEV polynomials adaptive spectral methods.

The $\mathcal{L}_\infty$ error can be computed along the space or time domains, according to:

$$\varepsilon(x) \stackrel{\text{def}}{:=} \sup_{t\in[0,\tau]} \left| u_{\text{ref}}(x,t) - u_{\text{num}}(x,t) \right|,$$

$$\varepsilon(t) \stackrel{\text{def}}{:=} \sup_{x\in[0,L]} \left| u_{\text{ref}}(x,t) - u_{\text{num}}(x,t) \right|.$$

When dealing with two fields u and v, as it is the case for the heat and moisture transfer, the $\mathcal{L}_\infty$ error is computed using:

$$\varepsilon \stackrel{\text{def}}{:=} \max\left\{ \left|\left| u_{\text{ref}} - u_{\text{num}} \right|\right|_\infty, \left|\left| v_{\text{ref}} - v_{\text{num}} \right|\right|_\infty \right\}.$$

4. Numerical application

4.1. Linear case

A linear heat ad moisture transfer problem is first considered to confirm the features of the proposed explicit scheme. The material length is $L = 0.1\,\mathrm{m}$. The hygrothermal properties of the material are $c_M = 6.1 \cdot 10^{-2}\ \mathrm{s^2/m^2}$, $k_M = 5.47 \cdot 10^{-10}\ \mathrm{s}$, $c_{TT} = 8.61 \cdot 10^{5}\ \mathrm{W.s/(K.m^3)}$, $c_{TM} = 5.09 \cdot 10^{3}\ \mathrm{W.s^3/(kg.m^2)}$, $k_{TT} = 3.87 \cdot 10^{-1}\ \mathrm{W/(m.K)}$ and $k_{TM} = 1.53 \cdot 10^{-2}\ \mathrm{W.s^2/kg}$. It corresponds to the properties of the load bear material for $T = 20\ °\mathrm{C}$ and $\phi = 50\ \%$ [13, 15]. At $t = 0\ \mathrm{h}$, the material has uniform temperature $T_i = 20\ °\mathrm{C}$ and relative humidity $\phi_i = 50\ \%$ fields. The boundary conditions, represented by the relative humidity ϕ and temperature T, are given in Figure 2. They oscillate between dry and moist states during 120 hours, allowing not to reach the steady state. No additional source term is considered for the moment. The convective mass and heat transfer coefficients are set to $h_M = 2 \cdot 10^{-7}\ \mathrm{s/m}$, $h_T = 25\ \mathrm{W/(m^2.K)}$ and $h_M = 3 \cdot 10^{-8}\ \mathrm{s/m}$, $h_T = 8\ \mathrm{W/(m^2.K)}$, for the left and right boundary conditions, respectively. The dimensionless numerical values of this case are provided in B.

The solution of the problem has been first computed for a discretisation $\Delta x^\star = 10^{-2}$ and $\Delta t^\star = 10^{-4}$, respecting the CFL condition. Physically, those values correspond to $\Delta x = 1\ \mathrm{mm}$ and $\Delta t = 3.6\ \mathrm{s}$. The physical phenomena are thus well represented, as illustrated in Figure 3. The field variations follow the boundary conditions. A good agreement is noticed between the three numerical schemes and the reference solution. Furthermore, the temperature and relative humidity profiles are shown in Figure 4 for $t = 10\ \mathrm{h}$, $t = 20\ \mathrm{h}$ and $t = 40\ \mathrm{h}$. All numerical methods give accurate results as illustrated with the $\mathcal{L}_\infty$ error, calculated as a function of x, in Figures 5(a) and 5(b). The numerical methods have the same accuracy of order $\varepsilon = 5 \cdot 10^{-5}$.

A numerical analysis of the behaviour of the three numerical schemes has been carried out for different values of the temporal discretisation Δt. The spatial discretisation is maintained to $\Delta x^\star = 10^{-2}$. Results of the $\mathcal{L}_\infty$ error ε are shown in Figures 6(b) and 6(a), for the temperature and the relative humidity, respectively. As expected, the explicit Euler scheme enables to compute the solution as far as the CFL condition is respected. The stability condition has a slightly higher constraint for the heat transfer equation Eq. (2.5a), $\Delta t^\star \leqslant 3 \cdot 10^{-4}$, than for the moisture equation Eq. (2.5b), $\Delta t^\star \leqslant 4 \cdot 10^{-3}$. As Eq. (2.5) is a system of weakly coupled linear equations, even if the CFL of the heat transfer equation Eq. (2.5a) is not respected, the solution of the moisture transfer equation Eq. (2.5b) can be computed (until its own CFL condition is met). The implicit Euler and Dufort–Frankel schemes are unconditionally stable and enable to compute the solution after the CFL limit. It also confirms that the Dufort–Frankel scheme is second-order accurate in time $\mathcal{O}(\Delta t^2)$ while the implicit Euler is first-order accurate in time $\mathcal{O}(\Delta t)$. The error ε reaches a lower bound, corresponding to the constant absolute accuracy of the case.

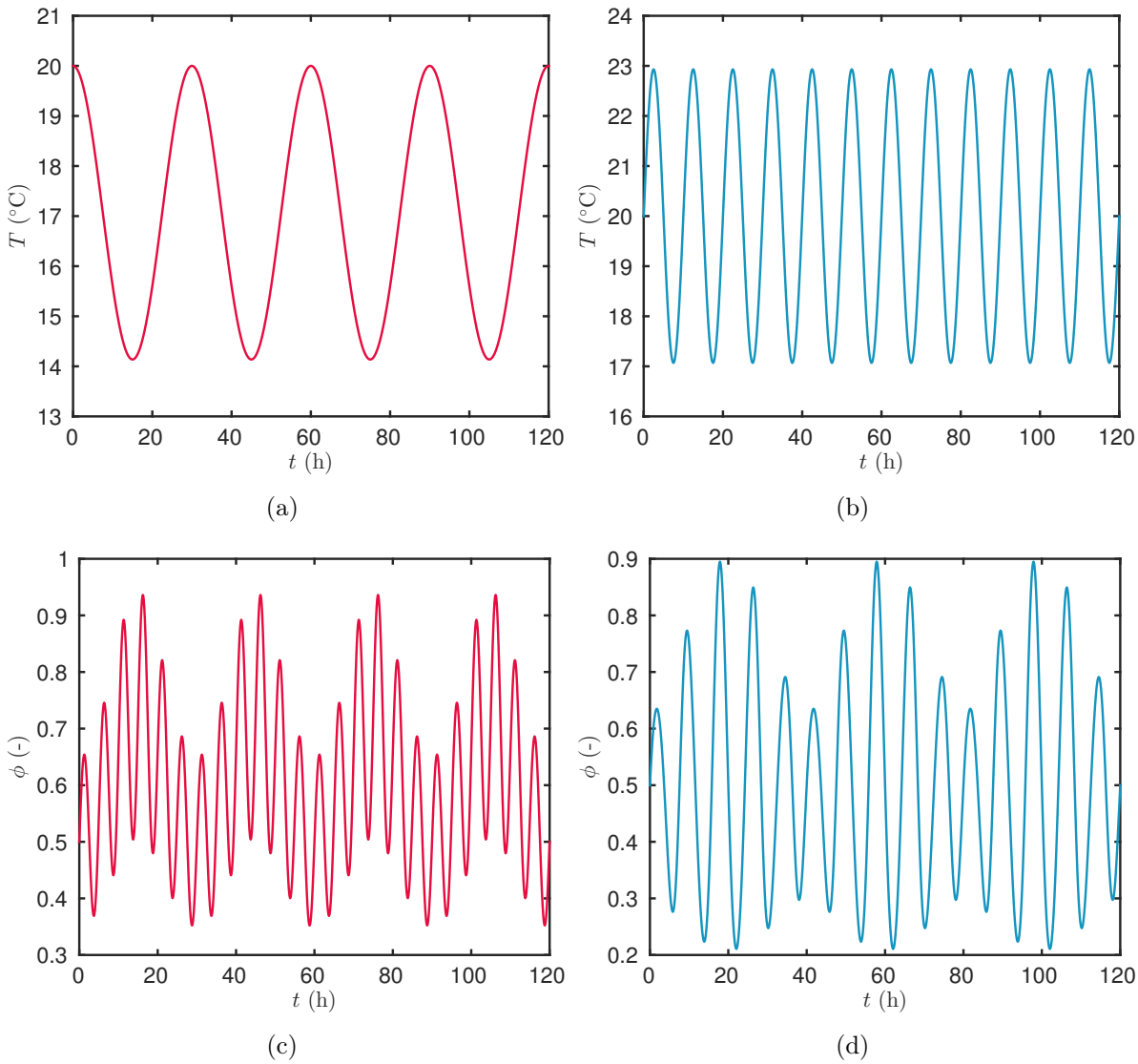

Figure 2. *Boundary conditions at* $x = 0$ m *(a,c) and* $x = 0.1$ m *(b,d).*

4.2. Nonlinear case

As heat and moisture transfer are strongly nonlinear due to the variation of the material properties with the field, a second case study is investigated considering these effects. The same boundary conditions, given in Figure 2, with equivalent convective mass and heat transfer coefficients, are taken into account. The hygrothermal material properties corresponds to a load bearing material, similar to the one considered in [12, 13, 15]. At $t = 0$ h, the material has uniform temperature $T_i = 20$ °C and relative humidity $\phi_i = 50$ % fields.

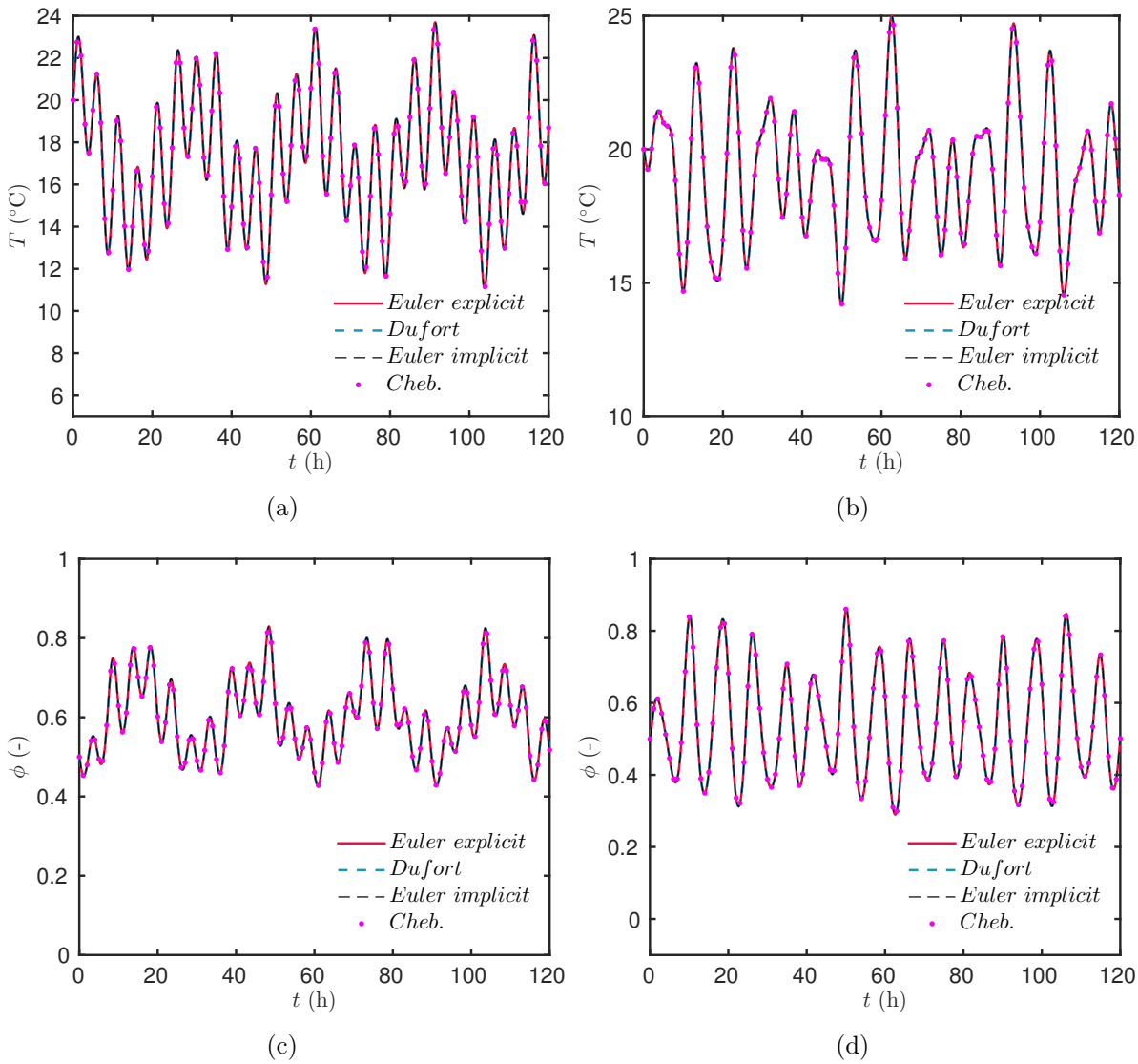

Figure 3. *Time evolution of the temperature and relative humidity at* $x = 0$ m *(a,c) and* $x = 0.1$ m *(b,d).*

As for the previous linear case study, the solution was computed using three numerical schemes, considering a spatial discretisation parameter $\Delta x^\star = 10^{-2}$. For the time domain, the discretisation parameter equals $\Delta t^\star = 10^{-3}$ for the Dufort–Frankel and implicit Euler scheme. A tolerance $\eta \leqslant 10^{-2}\ \Delta t^\star$ has been used for the convergence of the sub-iterations of the implicit scheme, using a fixed-point algorithm. For the explicit Euler scheme, a time discretisation $\Delta t^\star = 10^{-5}$ has been used, to respect the CFL stability condition. The latter has been computed using for the heat transfer equation

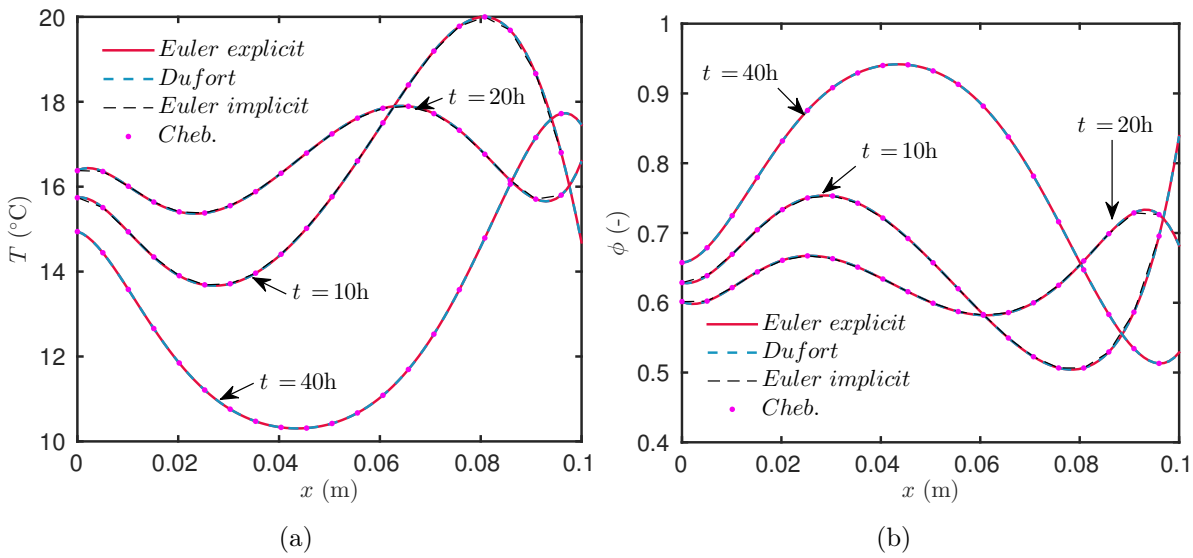

Figure 4. *Temperature and relative humidity profiles at* $t = 10$ h, $t = 20$ h *and* $t = 40$ h .

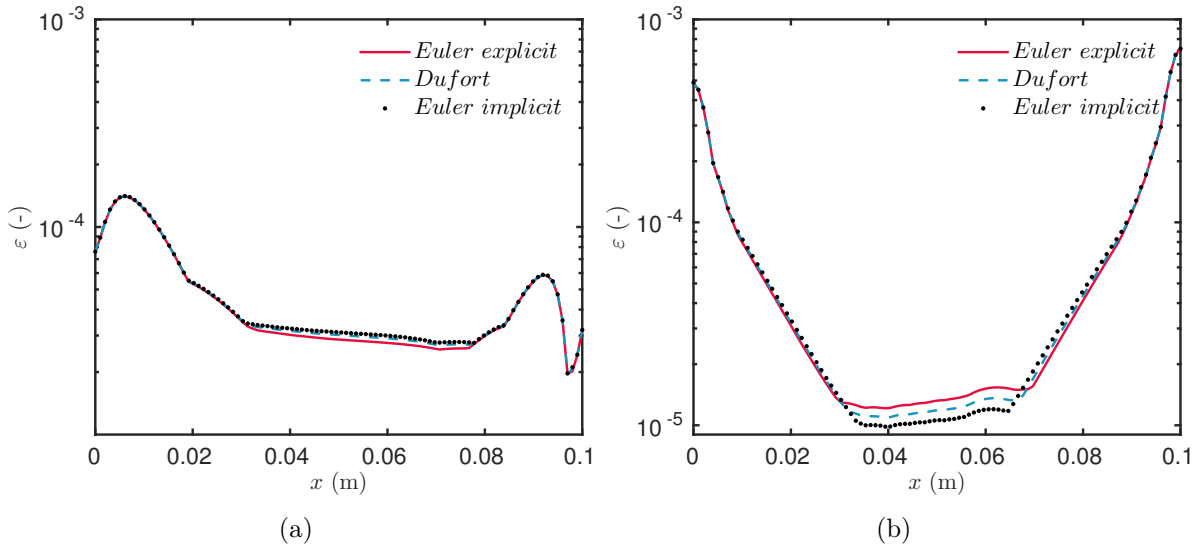

Figure 5. $\mathcal{L}_\infty$ *error between the reference solution and the ones computed with the numerical schemes, for temperature (a) and relative humidity (b).*

Eq. (2.5a):

$$\Delta t^\star \leqslant \frac{\left(\Delta x^\star\right)^2}{2} \min_{u,v} \left\{ \frac{c^\star_{TT}(u,v)}{\mathrm{Fo}_{TT}\, k^\star_{TT}(u,v)}, \frac{c^\star_{TT}(u,v)}{\mathrm{Fo}_{TM}\, k^\star_{TM}(u,v)}, \frac{c^\star_{TT}(u,v)\, c^\star_{M}(u,v)}{c^\star_{TM}(u,v)\, \gamma\, \mathrm{Fo}_{M}\, k^\star_{M}(u,v)} \right\}, \tag{4.1}$$

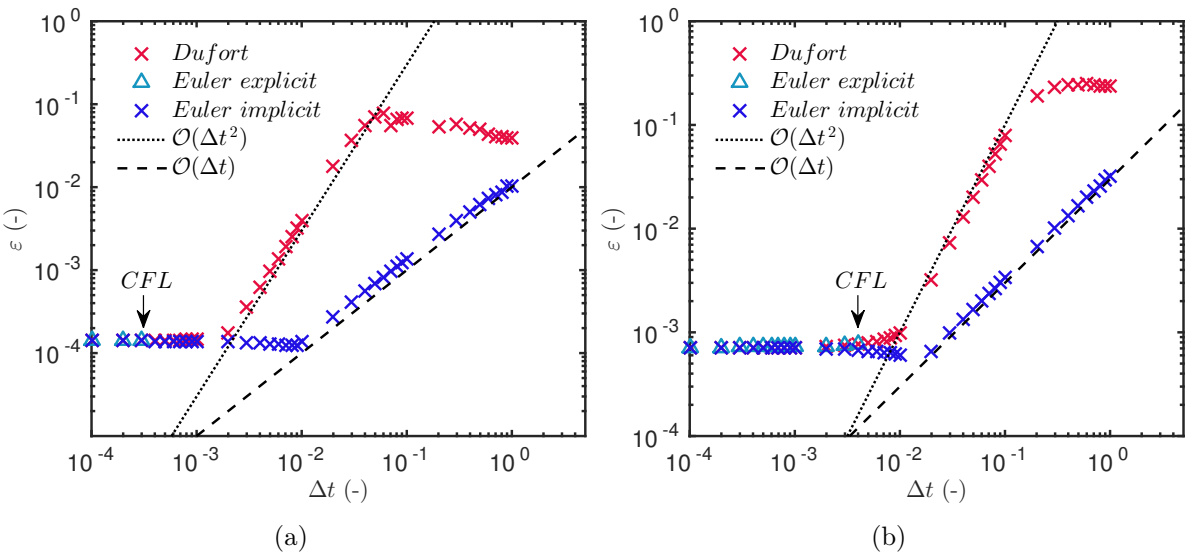

Figure 6. *$\mathcal{L}_\infty$ error as a function of Δt for the implicit* Euler, *explicit* Euler *and* Dufort–Frankel *schemes for temperature T (a) and relative humidity ϕ (b).*

and for the mass transfer equation Eq. (2.5b):

$$\Delta t^\star \leqslant \frac{\left(\Delta x^\star\right)^2}{2} \min_{u,v} \left\{ \frac{c_M^\star(u,v)}{\mathrm{Fo}_M\, k_M^\star(u,v)} \right\}, \tag{4.2}$$

which give the numerical values of $\Delta t^\star \leqslant 3 \cdot 10^{-4}$ and $\Delta t^\star \leqslant 7.4 \cdot 10^{-5}$, corresponding to physical values of $\Delta t^\star \leqslant 1.08$ s and $\Delta t^\star \leqslant 0.2$ s, respectively. It can be noted that the stability of the coupled equation is given by the moisture equation stability.

The time evolution of the fields is presented in Figure 7, showing a good agreement between the solution of each numerical scheme. The coupling effect between heat and mass transfer can be specially noted in Figure 7(a). The temperature at $x = 0$ m varies according to both frequencies of the left side air temperature and relative humidity, illustrated in Figures 2(c) and 2(a). The relative humidity rises until 98 % at $t = 40$ h, demonstrating that the material is solicited until the saturation state during the simulation. Figure 8 represents the field profiles at different time. We recall that the properties of the material of the previous linear case corresponds to the one of the load bear material for $T = 20$ °C and $\phi = 50$ %. Moreover, the same boundary conditions were taken into account. Thus, the influence of considering the material nonlinearities can be observed when comparing the results between both case studies. The temperature and relative humidity profiles are relatively different between Figures 4 and 8. The error between the reference solution and the ones computed with the different numerical scheme is given in Figures 9(b) and 9(a). It confirms that all the numerical schemes enable to compute an accurate solution, at the order of 10^{-4} for both fields and considered spatial and temporal discretisations.

For the implicit EULER and the explicit DUFORT–FRANKEL schemes, the CPU time has been calculated, using `Matlab` platform on a computer with Intel i7 CPU and 32GB of RAM, and shown in Table 2. The implicit scheme requires around 9 sub-iterations per time step to treat the nonlinearities of the problem. The DUFORT–FRANKEL approach computes directly the solution and therefore has a reduced computational costs, around 15% of the implicit EULER scheme based algorithm.

A convergence study was also performed for the explicit EULER and the DUFORT–FRANKEL numerical schemes by fixing the discretisation parameter $\Delta x^\star = 10^{-2}$ and varying $\Delta t^\star$. Results are shown in Figure 10. As expected, the explicit EULER scheme was not able to compute a solution when the stability CFL condition is not respected (around $\Delta t^\star \leqslant 8 \cdot 10^{-5}$). The values computed from Eq. (4.1) and (4.2) are in accordance with the results from the convergence study. It also confirms that the DUFORT–FRANKEL scheme is unconditionally stable, as it computes a solution for any discretisation parameter $\Delta t^\star$. The error of the numerical scheme is second-order accurate in time $\mathcal{O}(\Delta t^2)$.

5. Whole-building hygrothermal model

5.1. Coupling the lumped air multizone model with the transfer through porous walls

The lumped multizone model divides the whole-building into N_z perfectly mixed air zones. For each zone, the evolutions of the air temperature T_a and the humidity ratio w_a are given by the equations [3, 4, 28]:

$$\rho_a V \left(c_{p,a} + c_{p,v} w_a \right) \frac{\mathrm{d}T_a}{\mathrm{d}t} = Q_\mathrm{o} + Q_\mathrm{v} + Q_\mathrm{inz} + \sum_{i=1}^{N_w} Q_{w,i}\,, \tag{5.1a}$$

$$\rho_a V \frac{\mathrm{d}w_a}{\mathrm{d}t} = G_\mathrm{o} + G_\mathrm{v} + G_\mathrm{inz} + \sum_{i=1}^{N_w} G_{w,i}\,. \tag{5.1b}$$

Besides the dependence of the air heat capacity on the humidity ratio, the right-hand terms of the room air energy balance equation (5.1a) can also be strongly dependent on the humidity ratio, which may lead to a highly nonlinear problem.

Equation (5.1b) can be expressed using the vapour pressure of the air zone $P_{v,a}$, by means of the following relation:

$$w_a = \frac{M_v}{M_a} \frac{P_{v,a}}{P_a - P_{v,a}} \simeq \frac{P_v}{P_v^\circ}$$

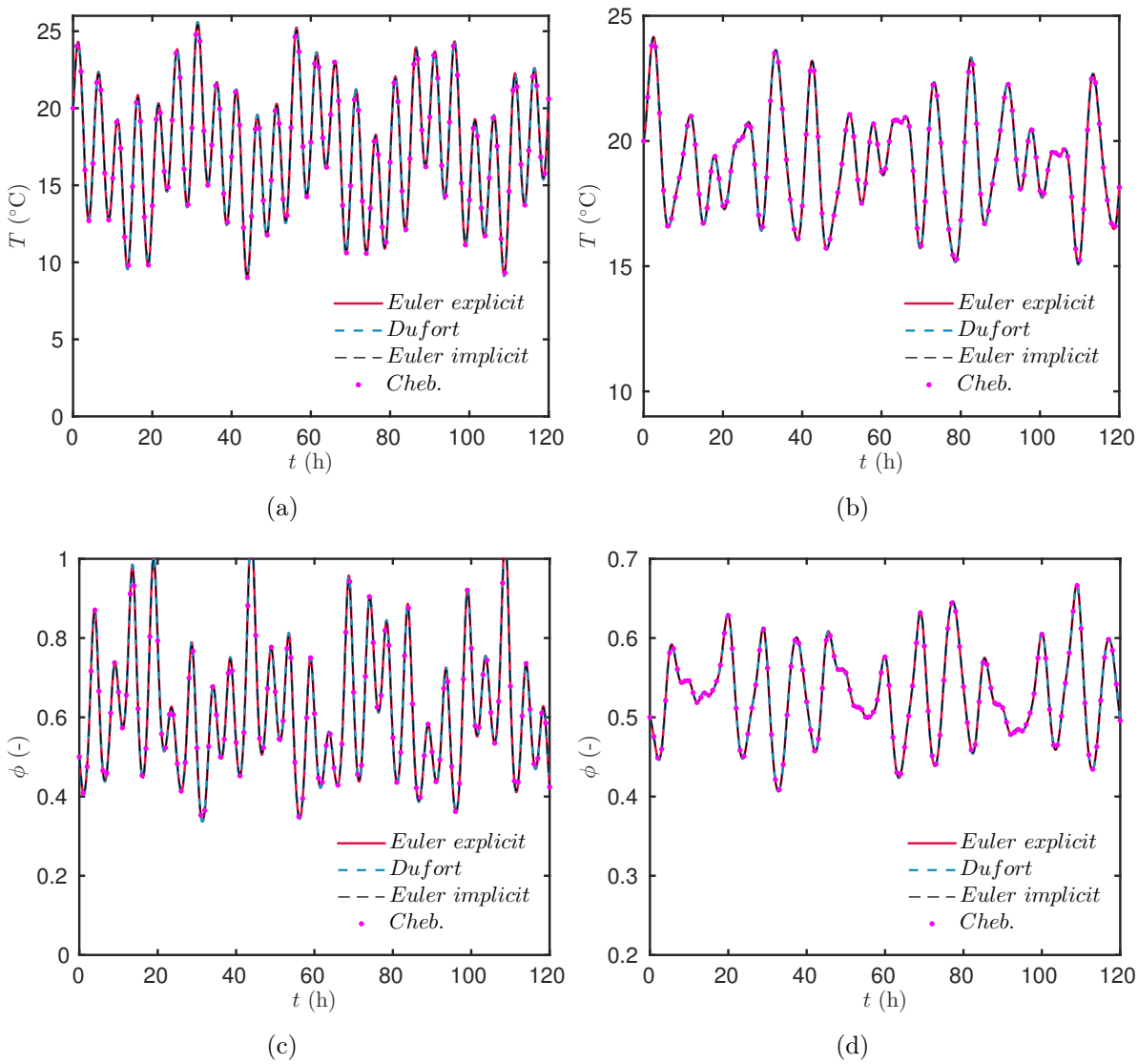

Figure 7. *Time evolution of the temperature and relative humidity at* $x = 0$ m *(a,c) and* $x = 0.1$ m *(b,d).*

where $P_v^\circ = 1.61 \cdot 10^5$ Pa. In addition, according to the notation used before, we have:

$$\kappa_{TT,0} \overset{\text{def}}{:=} \frac{\rho_a V c_{p,a}}{P_v^\circ}, \qquad \kappa_{TT,1} \overset{\text{def}}{:=} \frac{\rho_a V c_{p,v}}{P_v^\circ},$$

$$\kappa_{TT} \overset{\text{def}}{:=} \kappa_{TT,0} + \kappa_{TT,1} P_v, \qquad \kappa_M \overset{\text{def}}{:=} \rho_a V.$$

The terms G and Q are associated to occupants and their activities, denoted with the subscript o, as well as air flow from ventilation systems or infiltration, denoted with the subscript v. The sources due to interzone airflow are designated by Q_{inz} and G_{inz} correspondingly. Interested readers may find a detailed list of these sources and their physical

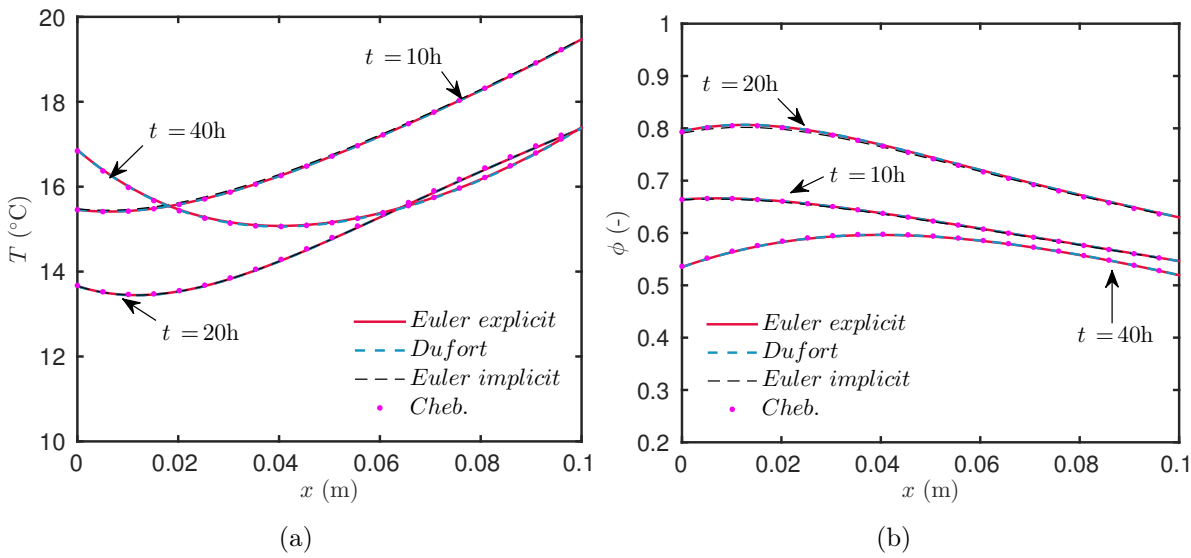

Figure 8. *Temperature and relative humidity profiles at* $t = 10$ h, $t = 20$ h *and* $t = 40$ h .

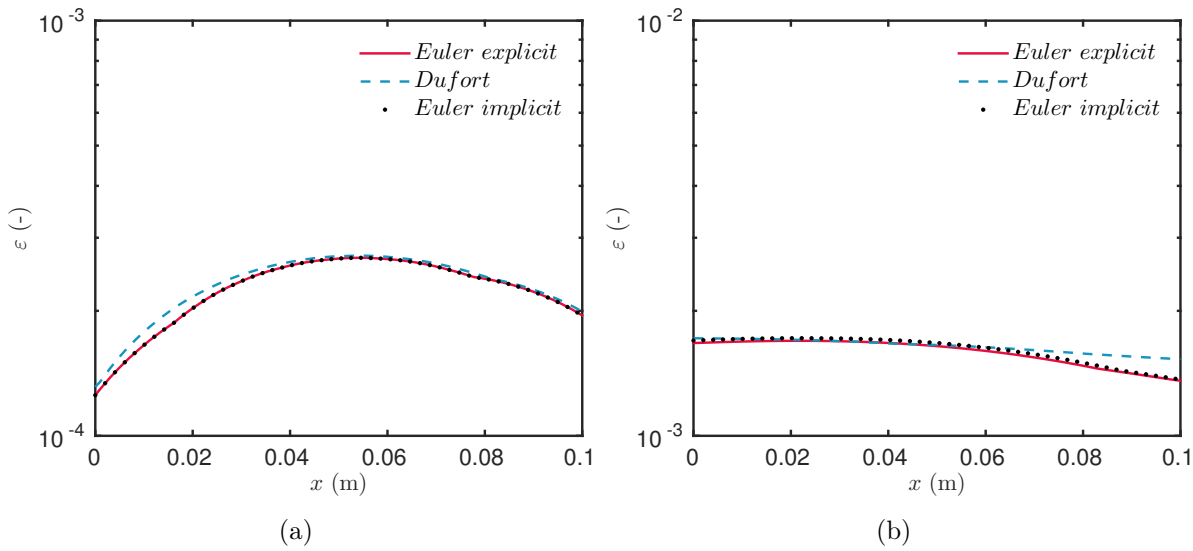

Figure 9. $\mathcal{L}_\infty$ *error between the reference solution and the ones computed with the numerical schemes, for temperature (a) and relative humidity (b).*

description in [9]. The first can be expressed as:

$$Q_o = L_v g_o(t), \qquad G_o = g_o(t),$$

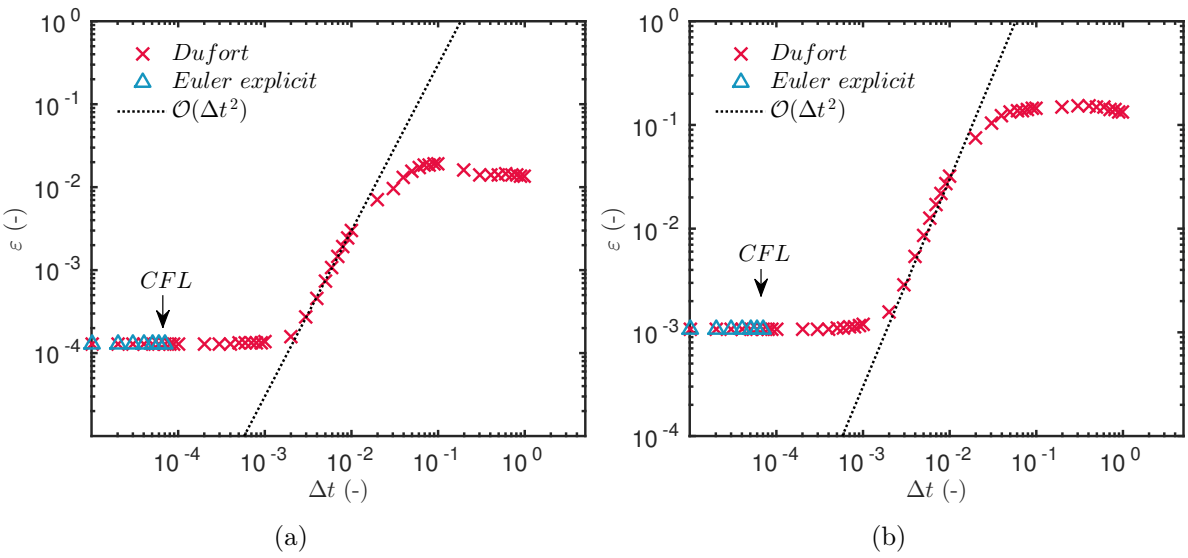

Figure 10. *$\mathcal{L}_\infty$ error as a function of Δt for the implicit* Euler, *explicit* Euler *and* Dufort–Frankel *schemes for temperature (a) and relative humidity (b).*

where g_{o} is the time variant vapour production. The sources due to ventilation system are written as:

$$\begin{aligned} Q_{\mathrm{v}} &= g_{\mathrm{v}} \left(c_w T_\infty - c_w T_a \right) + L_v g_{\mathrm{v}} \left(w_\infty - w_a \right), \\ G_{\mathrm{v}} &= g_{\mathrm{v}} \left(w_\infty - w_a \right), \end{aligned}$$

where g_{v} stands for the air flow rate due to ventilation and infiltration, T_∞ and w_∞ are the outside temperature and humidity ratio, and c_w the water heat capacity depending on the air temperature and humidity ratio. In a similar way, the sources due to an airflow g_{inz} between zones i and j are given by:

$$\begin{aligned} Q_{\mathrm{inz}} &= g_{\mathrm{inz}} \left(c_{wj} T_j - c_{wi} T_i \right) + L_v g_{\mathrm{inz}} \left(w_j - w_i \right), \\ G_{\mathrm{inz}} &= g_{\mathrm{inz}} \left(w_j - w_i \right). \end{aligned}$$

Here, a mean value of the latent heat of evaporation L_v, evaluated at the considered temperatures, is used for numerical application.The terms Q_w and G_w represent the mass and heat quantities exchanged between the air room and the the N_w bounding walls:

$$Q_w = h_T A \left(T_s - T_a \right) + L_v h_M A \left(P_{v,s} - P_{v,a} \right), \tag{5.2a}$$

$$G_w = h_M A \left(P_{v,s} - P_{v,a} \right), \tag{5.2b}$$

where A is the wall surface area. The terms T_s and $P_{v,s}$ are the wall surface temperature and vapour pressure. Considering Eq. (2.2), they correspond to $T_s = T(x=0)$ and $P_{v,s} = P_v(x=0)$ (with the adopted convention). Thus, the coupling between the wall model Eq. (2.2) and the lumped multizone model Eq. (5.1) is operated by the sources G_w and Q_w from Eq. (5.2).

The temperature and vapour pressure in the zone are initially at $T = T_i$ and $P_v = P_{v,i}$. To write a dimensionless formulation of Eq. (5.1), the following quantities are defined:

$$u_a \stackrel{\text{def}}{:=} \frac{T_a}{T_i}, \qquad v_a \stackrel{\text{def}}{:=} \frac{P_{v,a}}{P_{v,i}}, \qquad \kappa^\star_{aTT,1} \stackrel{\text{def}}{:=} \frac{\kappa_{TT,1}}{\kappa_{TT,0}} P_{v,i},$$

$$g^\star_o \stackrel{\text{def}}{:=} \frac{t_0}{P_{v,i} \cdot \kappa_M} g_o, \qquad q^\star_o \stackrel{\text{def}}{:=} \frac{t_0}{T_i \cdot \kappa_{TT,0}} L_v g_o, \qquad g^\star_v \stackrel{\text{def}}{:=} \frac{g_v t_0}{P^\circ_v \kappa_M},$$

$$q^\star_{v,1} \stackrel{\text{def}}{:=} \frac{c_w g_v t_0 P_{v,i}}{P^\circ_v \kappa_{TT,0}}, \qquad q^\star_{v,2} \stackrel{\text{def}}{:=} \frac{L_v g_v t_0 P_{v,i}}{P^\circ_v \kappa_{TT,0} T_i} \qquad g^\star_{inz} \stackrel{\text{def}}{:=} \frac{g_{inz} t_0}{P^\circ_v \kappa_M},$$

$$q^\star_{inz,1} \stackrel{\text{def}}{:=} \frac{c_w g_{inz} t_0 P_{v,i}}{P^\circ_v \kappa_{TT,0}}, \qquad q^\star_{inz,2} \stackrel{\text{def}}{:=} \frac{L_v g_{inz} t_0 P_{v,i}}{P^\circ_v \kappa_{TT,0} T_i} \qquad \theta_T \stackrel{\text{def}}{:=} \frac{k_{TT,0} \cdot A \cdot t_0}{L \cdot \kappa_{TT,0}},$$

$$\theta_M \stackrel{\text{def}}{:=} \frac{k_{M,0} \cdot A \cdot t_0}{L \cdot \kappa_M}$$

Thus, the dimensionless formulation of Eq. (5.1) can be written as:

$$\begin{aligned}
\left(1 + \kappa^\star_{aTT,1}\right)\frac{\mathrm{d}u_a}{\mathrm{d}t^\star} &= q^\star_o + q^\star_{v,1}\left(u_\infty v_\infty - u_a v_a\right) + q^\star_{v,2}\left(u_\infty - u_a\right) \\
&+ q^\star_{inz,1}\left(u_{a,2} v_{a,2} - u_a v_a\right) + q^\star_{inz,2}\left(u_{a,2} - u_a\right) \\
&+ \sum_{i=1}^{N_w} \mathrm{Bi}_{TT,i}\,\theta_{T,i}\left(u_i - u_a\right) + \mathrm{Bi}_{TM,i}\,\theta_{T,i}\left(v_i - v_a\right), \qquad (5.3a)\\
\frac{\mathrm{d}v_a}{\mathrm{d}t^\star} &= g^\star_o + g^\star_v\left(v_\infty - v_a\right) + g^\star_{inz}\left(v_{a,2} - v_a\right) \\
&+ \sum_{i=1}^{N_w} \mathrm{Bi}_{M,i}\,\theta_{M,i}\left(v_a - v_i\right). \qquad (5.3b)
\end{aligned}$$

The quantities u_∞, v_∞ and $u_{a,2}$, $v_{a,2}$ come from building outside (provided by weather data) and from the adjacent zone. The coupling between the wall model Eq. (2.5) and the lumped multizone model Eq. (5.3) is operated through the wall source terms. The dimensionless parameters Bi_{TT}, Bi_{TM} and Bi_M qualify the penetration of the heat and moisture through the wall according to the physical mechanism. The parameters $\theta_{T,i}$ and $\theta_{M,i}$ depend on the wall surface on the room air, providing the weighted contribution of the wall to the energy and moisture balances.

5.2. Implicit scheme for the whole-building energy simulation: problem statement

For the sake of simplicity and without loosing the generality, the coupling procedure is explained considering *only* the linear heat diffusion equation Eq. (3.1) for one wall model with the following boundary conditions for the surface in contact with the outside ($x = 0$)

and inside($x = 1$) air of the building:

$$\frac{\partial u}{\partial x} = \mathrm{Bi}_{TT}\left(u - u_\infty\right) \qquad x = 0\,, \tag{5.4a}$$

$$\frac{\partial u}{\partial x} = -\mathrm{Bi}_{TT}\left(u - u_a\right) \qquad x = 1\,. \tag{5.4b}$$

The room air energy conservation equation for the multizone model is expressed as:

$$\frac{\mathrm{d}u_a}{\mathrm{d}t} = Q + \mathrm{Bi}_{TT}\,\Theta_T\left(u - u_a\right), \tag{5.5}$$

Many whole-building models reported in the literature, such as MATCH [25], MOIST [5] and DOMUS [8, 19, 21], use implicit (Euler or Crank–Nicolson) approaches to solve these equations, mainly due to the unconditional stability property. Thus, using an Euler implicit approach, the discretisations of Eqs. (3.1), (5.4a), (5.4b) yield to:

$$\begin{aligned}
\frac{1}{\Delta t}\left(u_j^{n+1} - u_j^n\right) &= \frac{\nu}{\Delta x^2}\left(u_{j+1}^{n+1} - 2\,u_j^{n+1} + u_{j-1}^{n+1}\right),\\
\frac{1}{\Delta x}\left(u_1^{n+1} - u_0^{n+1}\right) &= \mathrm{Bi}_{TT}\left(u_0^{n+1} - u_\infty^{n+1}\right),\\
\frac{1}{\Delta x}\left(u_N^{n+1} - u_{N-1}^{n+1}\right) &= -\mathrm{Bi}_{TT}\left(u_N^{n+1} - u_a^{n+1}\right).
\end{aligned}$$

Therefore, at iteration t^n, solution u^{n+1}, of the wall model, is computed using the resolvent operator $\mathcal{R}^{\mathrm{w}}_{\mathrm{imp}}$ written as:

$$u^{n+1} = \mathcal{R}^{\mathrm{w}}_{\mathrm{imp}}\left(u^n,\, u_a^{n+1},\, u_\infty^{n+1}\right),$$

In the same way, the discretisation of Eq. (5.5) yields to:

$$\frac{1}{\Delta t}\left(u_a^{n+1} - u_a^n\right) = Q^{n+1} + \mathrm{Bi}_{TT}\,\Theta_T\left(u_N^{n+1} - u_a^{n+1}\right),$$

and, at iteration t^n, solution u_a^{n+1}, of the multizone model, is computed using the resolvent operator $\mathcal{R}^{\mathrm{a}}_{\mathrm{imp}}$ written as:

$$u_a^{n+1} = \mathcal{R}^{\mathrm{a}}_{\mathrm{imp}}\left(u_a^n,\, u^{n+1}\right).$$

By coupling the wall and the multizone models to perform a whole-building energy simulation, ones must solve at each time iteration the following system of equations:

$$u^{n+1} = \mathcal{R}^{\mathrm{w}}_{\mathrm{imp}}\left(u^n,\, u_a^{n+1},\, u_\infty^{n+1}\right), \tag{5.6a}$$

$$u_a^{n+1} = \mathcal{R}^{\mathrm{a}}_{\mathrm{imp}}\left(u_a^n,\, u^{n+1}\right). \tag{5.6b}$$

As the system Eq. (5.6) is nonlinear, it is not possible to solve it directly. Thus, $\left(u^{n+1},\, u_a^{n+1}\right)$ are computed using, for instance, a fixed point algorithm, until reaching a prescribed tolerance η, as illustrated in Alg. 1. The number of subiterations should increase with the number of walls considered in the whole-building model, when dealing with nonlinear models and when considering interzone airflows. Interested readers may report to [8] for more details on this problem statement. Indeed, authors investigate the influence of the time

step on the computational time of a whole-building simulation model, considering only heat transfer, for different numerical schemes and analytical solution.

$u^k = u^n$;
$u_a^k = u^n$;
while $\left\| u^{k+1} - u^k, u_a^{k+1} - u_a^k \right\| \geqslant \eta$ **do**
  $u^{k+1} = \mathcal{R}_{\text{imp}}^{\text{w}} \left(u^n, u_a^k, u_\infty^{n+1} \right)$;
  $u_a^{k+1} = \mathcal{R}_{\text{imp}}^{\text{a}} \left(u_a^n, u^{k+1} \right)$;
  $u^k = u^{k+1}$;
  $u_a^k = u_a^{k+1}$;
end
$u^{n+1} = u^{k+1}$;
$u_a^{n+1} = u_a^{k+1}$;

Algorithm 1: *Fixed point algorithm to compute* $\left(u^{n+1}, u_a^{n+1} \right)$ *, using implicit numerical schemes, within the framework of whole-building simulation energy.*

5.3. Improved explicit schemes for the whole-building energy simulations

Using the improved explicit Dufort–Frankel scheme, results from Section 3.3 have shown that the discretisation of Eqs. (3.1), (5.4a), (5.4b) is given by:

$$u_j^{n+1} = \frac{1 - \lambda}{1 + \lambda} u_j^{n-1} + \frac{\lambda}{1 + \lambda} \left(u_{j+1}^n + u_{j-1}^n \right).$$

Moreover, to solve equation Eq. (5.5), we get the scheme:

$$\frac{1}{\Delta t} \left(u_a^{n+1} - u_a^n \right) = Q^n + \text{Bi}_{TT} \Theta_T \left(u_N^n - u_a^n \right).$$

Therefore, by coupling the wall and the multizone models, at each time iteration, the solution of the equations is directly computed:

$$u^{n+1} = \mathcal{R}_{\text{exp}}^{\text{w}} \left(u^n, u_a^n, u_\infty^n \right), \tag{5.7a}$$

$$u_a^{n+1} = \mathcal{R}_{\text{exp}}^{\text{a}} \left(u_a^n, u^n \right). \tag{5.7b}$$

Thus, the use of improved explicit schemes, such as the Dufort–Frankel one, is particularly advantageous to avoid subiterations at each time step to compute the dependent variable fields. In addition, the numerical property of unconditional stability avoids any limitation on the values of the time step Δt, which is chosen only according to the characteristic time of the physical phenomena [12].

6. Numerical application

6.1. Linear case

A single zone, surrounded by four walls is considered, as illustrated in Figure 11(a). The physical properties of the materials constituting the walls are linear and shown in Table 1. Their dimensionless values are provided in B. The convective mass and heat transfer coefficients are set to $h_M = 3 \cdot 10^{-8}$ s/m and $h_T = 8$ W/(m^2.K) between the inside air zone and the walls. It is assumed that no transfer occurs through the ceiling and the floor. The zone has a floor area of 18 m^2 and a volume of 54 m^3. The room is subjected to a constant moisture load of 25 g/h with an increase of 400 g/h from 6 h to 9 h each day. External air enters the room through ventilation and infiltrations at a constant rate of $g_v = 0.5$ h^{-1}. There are no radiative heat exchange among the walls. The initial temperature and relative humidity in the zone are $T_i = 20$ °C and $\phi_i = 50$ %, respectively. The outside boundary conditions T_∞ and ϕ_∞ are given in Figures 11(b) and 11(c). The convective transfer coefficients between the walls and the outside conditions are also provided in Table 1. For this case, neither radiation or rain sources are considered for the boundary conditions. The whole simulation is performed for 80 h. The walls and zone fields are computed using the implicit Euler and explicit Dufort–Frankel schemes. The explicit Euler scheme has stability restrictions and, to our knowledge, is not commonly used in building simulation programs. Thus, it was not included in this case study. The space and time discretisation parameters are $\Delta x^\star = 10^{-2}$ and $\Delta t^\star = 10^{-3}$, corresponding, from a physical point of view, to $\Delta x = 10^{-3}$ m and $\Delta t = 3.6$ s, and each solution is compared with the one computed using the `Chebfun` package for `Matlab`.

The time evolution of the temperature and relative humidity for different walls and for the air zone are given in Figures 12 and 13. The solutions computed with the Euler and Dufort–Frankel schemes are in very good agreement with the ones from `Chebfun`. As for the material properties of the wall, differences between the field evolution can be observed. Particularly, in Figures 12(a) and 12(c), the increase and decrease of temperature at $x = 0$ m are higher for the Eastern wall than for the Northern one. It is due to a higher Biot number for the latter: $\mathrm{Bi}_{TT} = 3.1$ against $\mathrm{Bi}_{TT} = 1.7$. In Figures 13(a) and 13(b) the increase and decrease of relative humidity are different at $x = 0$ m between the Northern and Southern walls. In Figure 13(d), a slight increase of relative humidity due to moisture generation in the zone from 6 to 9 h can be observed. The $\mathcal{L}_\infty$ in space x has been computed for the fields in the four walls, as illustrated in Figure 14(a). Moreover, the $\mathcal{L}_\infty$ error with respect to t for the fields in the zone is given in Figure 14(b). The error is approximately $\mathcal{O}(10^{-4})$ for both models, proving the accuracy of the solution computed with the implicit Euler and explicit Dufort–Frankel schemes. For each scheme, the CPU time has been calculated, using `Matlab` platform on a computer with Intel i7 CPU and 32GB of RAM, and is shown in Table 2. The explicit Dufort–Frankel scheme requires less than 10% of the time needed for the implicit Euler one, to compute the solution. This difference is due to the sub-iterations needed to solve the nonlinear system composed by equations of the wall and zone models. In this case, a fixed-point algorithm

Parameter	*North Wall*	*South Wall*	*East and West walls*
c_M $(\mathrm{s}^2/\mathrm{m}^2)$	$1.82 \cdot 10^{-2}$	$1.18 \cdot 10^{-1}$	$6.09 \cdot 10^{-2}$
k_M (s)	$5.89 \cdot 10^{-9}$	$2.92 \cdot 10^{-8}$	$5.47 \cdot 10^{-9}$
c_{TT} $\left(\mathrm{W \cdot s}/(\mathrm{K \cdot m}^3)\right)$	$7.7 \cdot 10^5$	$1.28 \cdot 10^6$	$8.61 \cdot 10^5$
k_{TT} $\left(\mathrm{W}/(\mathrm{m \cdot K})\right)$	$2.94 \cdot 10^{-1}$	$8.41 \cdot 10^{-1}$	$3.87 \cdot 10^{-1}$
c_{TM} $\left(\mathrm{W \cdot s}^3/(\mathrm{kg \cdot m}^2)\right)$	$1.52 \cdot 10^3$	$9.88 \cdot 10^3$	$5.09 \cdot 10^3$
k_{TM} $\left(\mathrm{W \cdot s}^2/\mathrm{kg}\right)$	$1.59 \cdot 10^{-2}$	$2.96 \cdot 10^{-3}$	$1.53 \cdot 10^{-2}$
A (m^2)	18	18	9
h_T $\left(\mathrm{W}/(\mathrm{m}^2 \cdot \mathrm{K})\right)$	5	25	12
h_M (s/m)	$2 \cdot 10^{-7}$	$8 \cdot 10^{-7}$	$4 \cdot 10^{-7}$

Table 1. *Wall material properties.*

with tolerance parameter $\eta = 0.01 \cdot \Delta t$, as the one illustrated in Algorithm 1, has been used. As emphasized in Figure 15, this algorithm required almost three sub-iterations to compute the solution at each time iteration.

A convergence study of the whole-building model has been carried out by fixing the space discretisation to $\Delta x = 10^{-2}$ and varying the time discretisation. Results are reported in Figures 16(a) and 16(b), for each field. The error with the reference solution has been computed for each field (temperature and relative humidity) and for each model (wall and zone). As expected, the explicit Dufort–Frankel scheme is second-order accurate in time $\mathcal{O}(\Delta t^2)$ for both models and both fields. On the contrary, the implicit Euler scheme is first-order accurate in time. It can be noted that the wall model reach a constant absolute accuracy lower than the one for the zone.

6.2. Nonlinear case

Previous case study considered a single zone building hygrothermal simulation with linear wall material properties. It enabled to enhance the sub-iterations required using implicit Euler scheme when coupling the wall and zone models. The present case focus on a bi-zone building, as shown in Figure 17(a), and take into account the variation of the wall material properties with temperature and relative humidity, such as the ones used in Section 4.2. Furthermore, the radiative heat exchanged among the room air surfaces are included. All the inside walls have an emissivity $\epsilon = 0.5$ except the wall 7, which have a

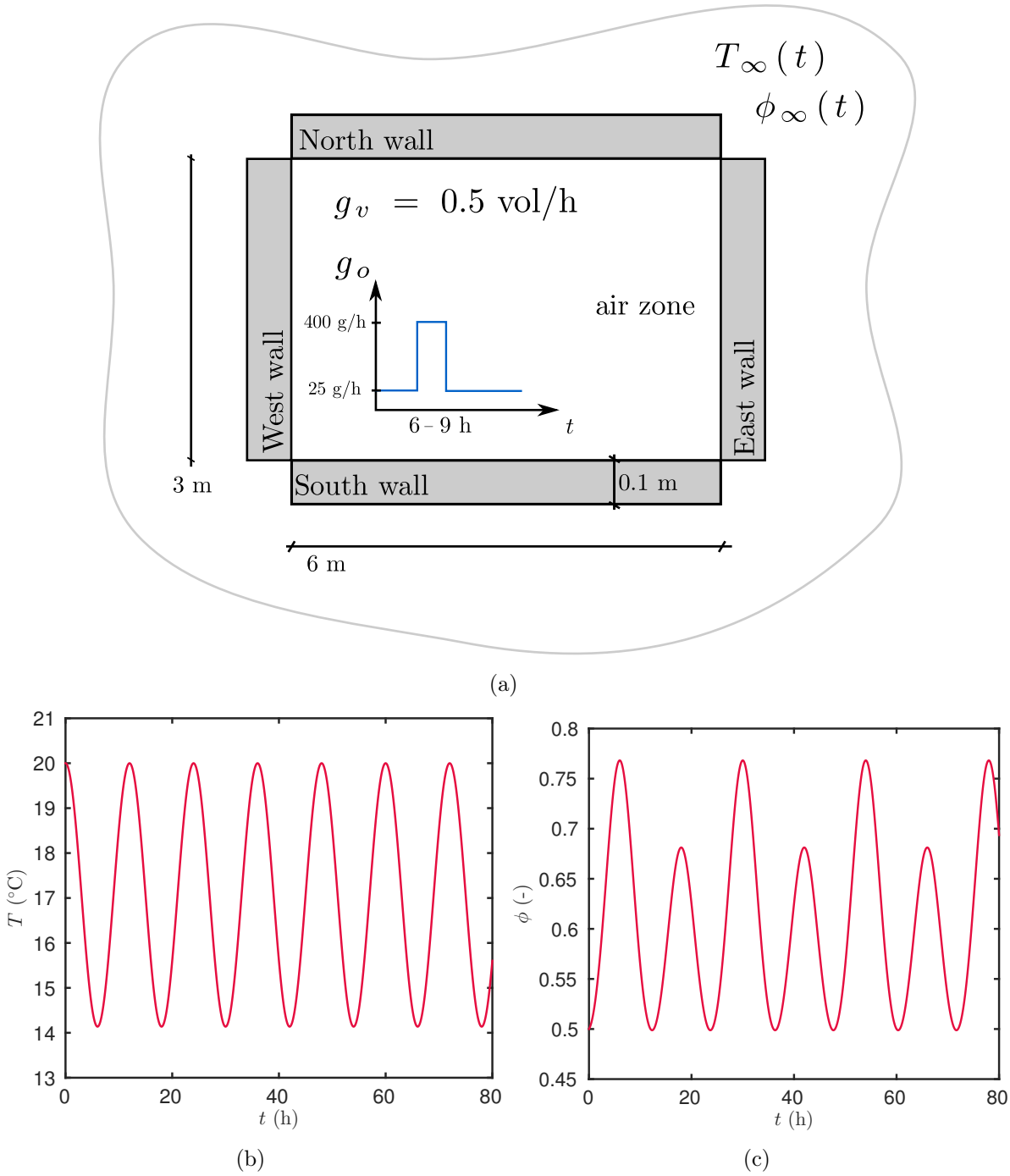

Figure 11. *Illustration of the case study (a) and the boundary conditions T_∞ (b) and ϕ_∞ (c) for the linear case.*

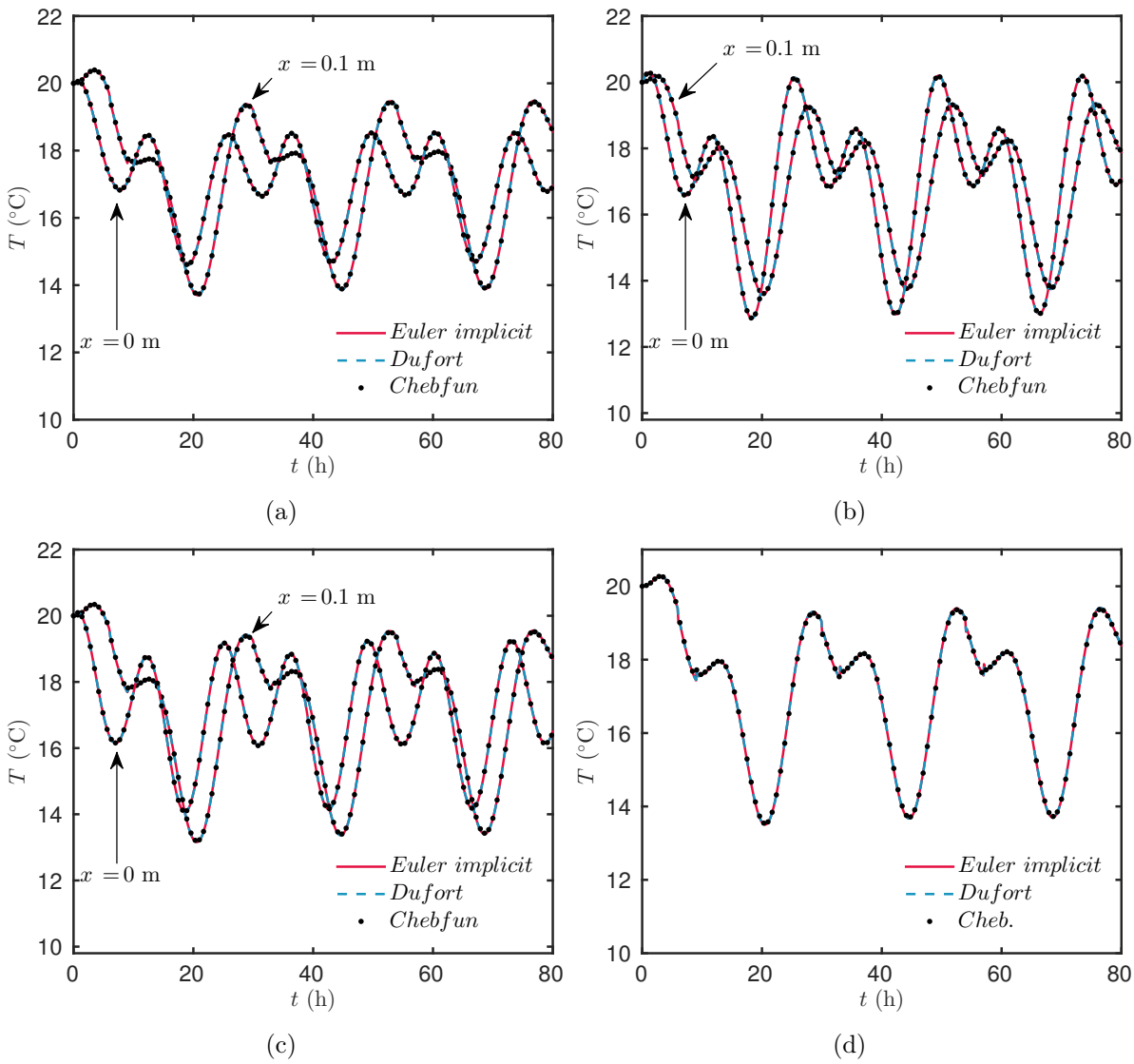

Figure 12. *Evolution of the temperature for the North (a), South (b) and East (c) walls and for the air zone (d) for the linear case.*

higher value $\epsilon = 0.9$. The view factor is set to $s = 0.2$. Incident radiation is considered for the outside boundary condition, shown in Figure 17(b). An airflow of $g_{\text{inz}} = 0.3\ \text{h}^{-1}$ occurs between both zones. Only zone 1 is subjected to moisture sources due to occupants and to air ventilation. Zone 2 receives a heat source $q_h = 500$ W from 3 to 4 h. The other parameters have the same numerical values as in the previous case study. This case study was designed in order to enforce the nonlinearities of the whole-building model, to increase the sub-iterations of the implicit Euler approach and thus enhance the efficiency of the Dufort–Frankel explicit scheme. The solution is computed using both schemes, with a time and space discretisations $\Delta t^\star = 10^{-3}$ and $\Delta x^\star = 10^{-2}$, equivalent to $\Delta x = 10^{-3}$ m and $\Delta t = 3.6$ s.

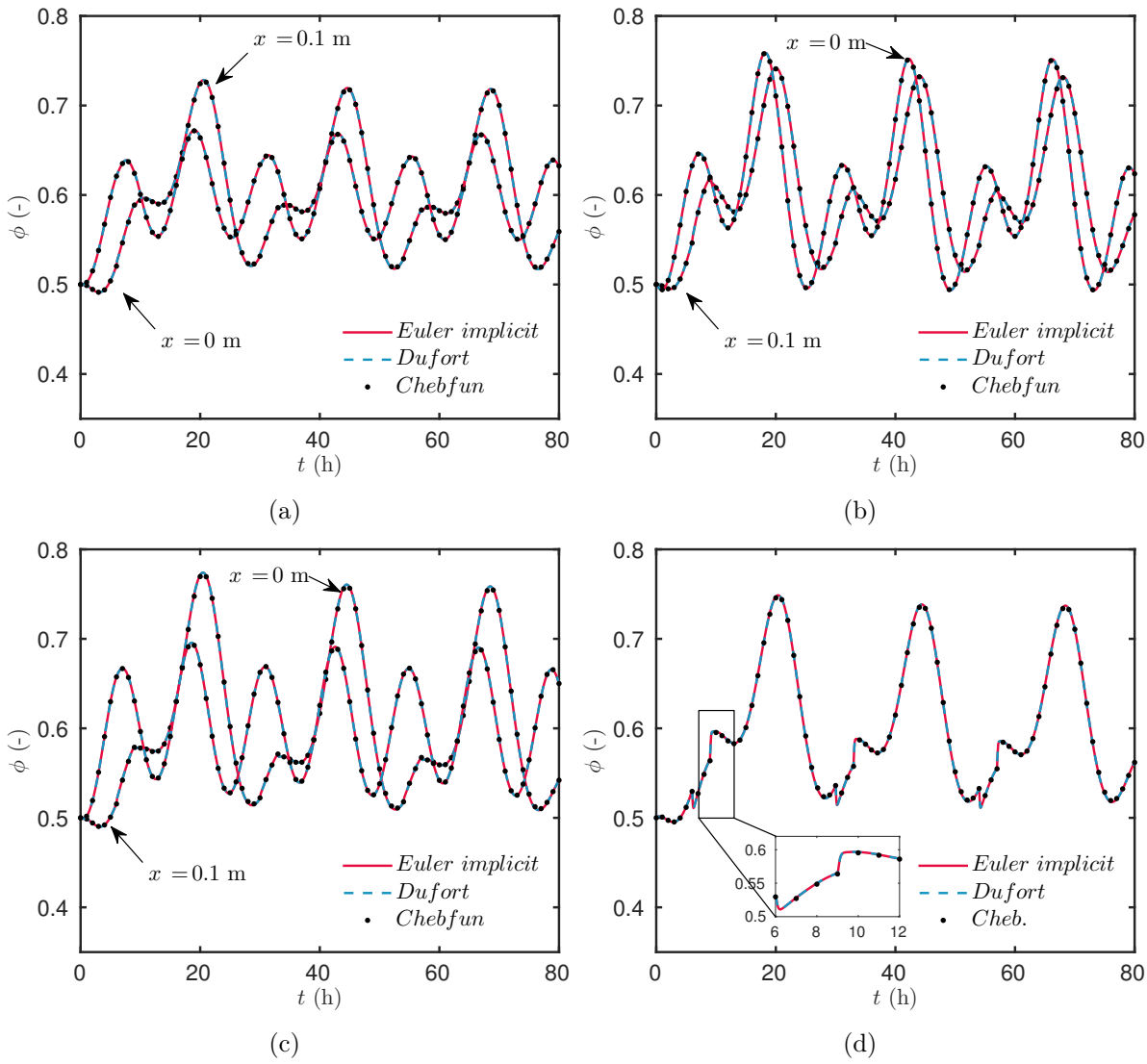

Figure 13. *Evolution of the relative humidity for the North (a), South (b) and East (c) walls and for the air zone (d) for the linear case.*

Figures 18(a) and 18(b) present the time evolution of the dependent variable fields for the wall 1, showing a very good agreement among the three solutions. By comparing Figures 12(a), 13(a), 18(a) and 18(b), the effect of considering nonlinear material properties can be observed. Similar observations can be done by analysing Figures 19(a), 19(b), 19(c) and 19(d). The moisture production in zone 1 is enhanced by an increase of the relative humidity from 6 to 9 h. As the moisture generation only occurs in this zone, there is no increase of the relative humidity in zone 2 due to this phenomena. Moreover, the heat production in zone 2 is highlighted from 2 to 6 h. The temperature reach 24 °C. A slight increase is observable in zone 1 during this period due to the heat generation in zone 2 and

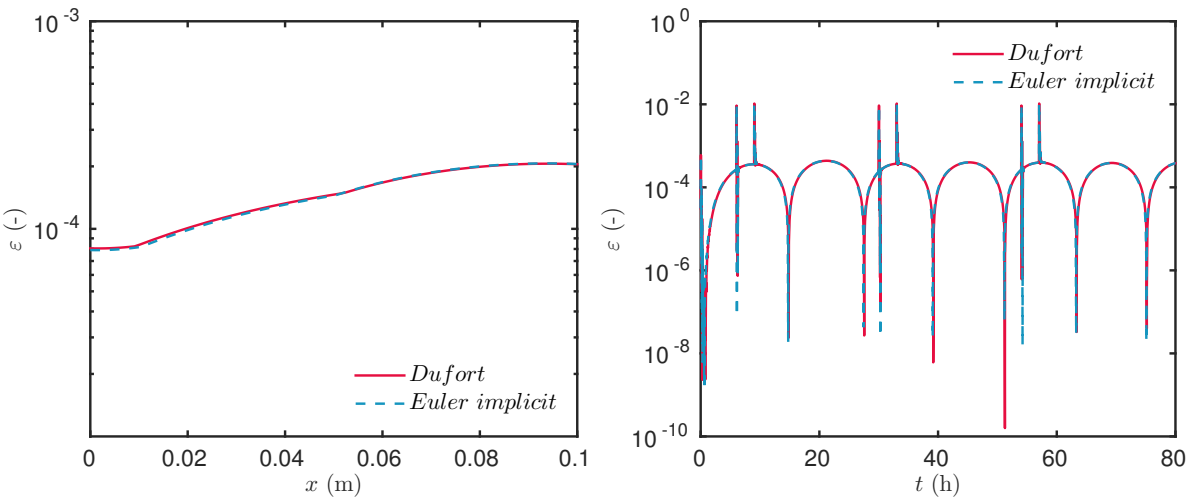

(a) (b)

Figure 14. *Error of the solutions computed with the implicit* Euler *and explicit* Dufort–Frankel *schemes for the walls (a) and for the air zone (b) for the linear case.*

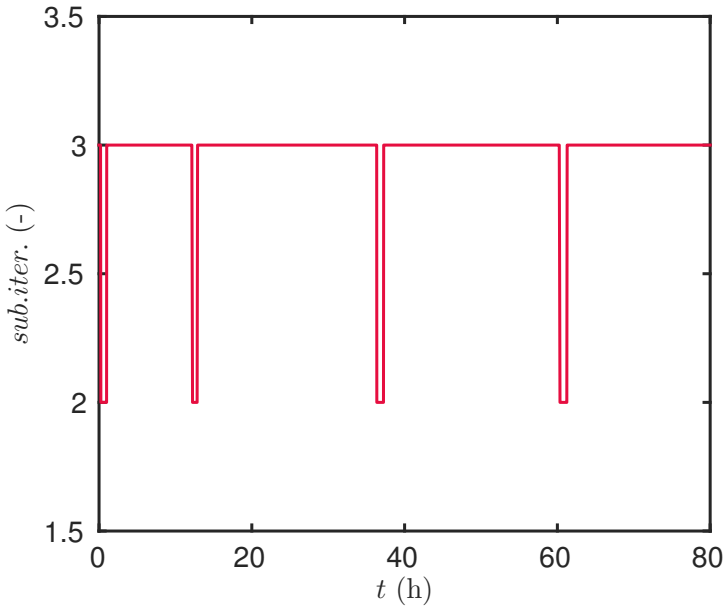

Figure 15. *Sub-iterations required for the implicit* Euler *scheme compute the solution of the whole-building energy model for the linear case.*

to the airflow between both zones. The error with the reference solution is of the order of $\mathcal{O}(10^{-4})$ for the wall and zone fields, as shown in Figures 20(a) and 20(b).

By considering nonlinear wall material properties, the implicit Euler scheme require more sub-iterations at each time iteration as illustrated in Figure 21. In the previous

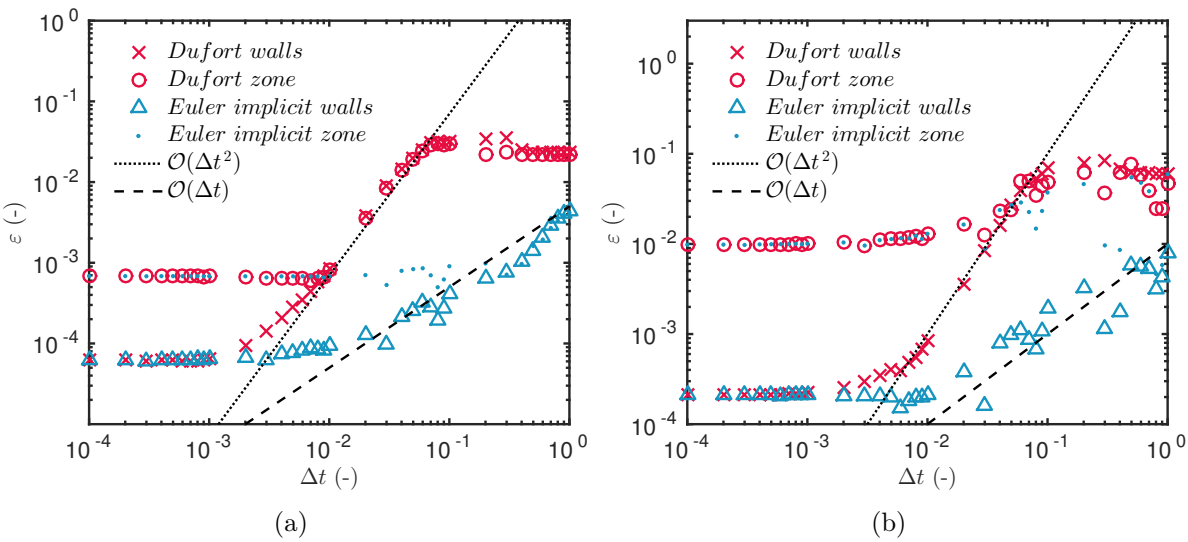

Figure 16. $\mathcal{L}_\infty$ error as a function of Δt for the implicit EULER and explicit DUFORT–FRANKEL schemes for temperature (a) and relative humidity (b) for the linear case.

linear case study, the algorithm required around 3 iterations whereas for the present case, it needs at least 6 to achieve the same accuracy. Therefore, the CPU time of the implicit EULER scheme to compute the numerical solution increases, as reported in Table 2. As no sub-iterations are necessary for the explicit DUFORT–FRANKEL scheme, the computation gain rises compared to the previous case study. It needs only 5 % of the CPU time of the implicit EULER scheme. These gains might considerably increase when considering highly nonlinear phenomena such as driving rain and iteration with HVAC systems [1].

7. Conclusion

Notwithstanding implicit methods are extensively used in building simulation codes, due to their stability conditions, they may require important extra computation when dealing with highly nonlinear problems such as the combined heat and moisture transfer through porous building elements or when the whole-building is simulated, demanding a perfect synchronism. In this way, this study aimed at exploring the use of the improved explicit DUFORT–FRANKEL scheme first for computing the solution of a highly coupled heat and moisture transfer problem through a porous building element. Both Linear and nonlinear material properties were considered and the advantages of this approach were highlighted to perform whole-building hygrothermal simulation. Both single-zone and a two-zone building models were analysed for the sake of simplicity.

The results have shown that the DUFORT–FRANKEL scheme enables to compute an accurate solution. The solution was compared to the one computed with the implicit and explicit EULER schemes and to a reference solution obtained using the `Matlab` *Chebfun*

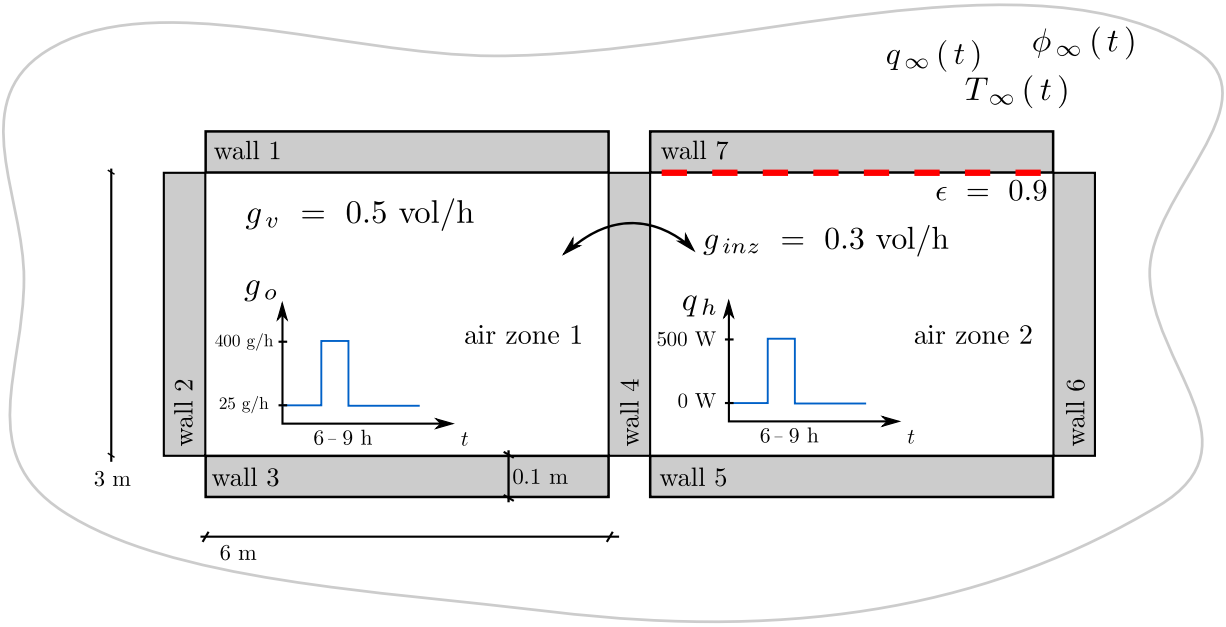

(a)

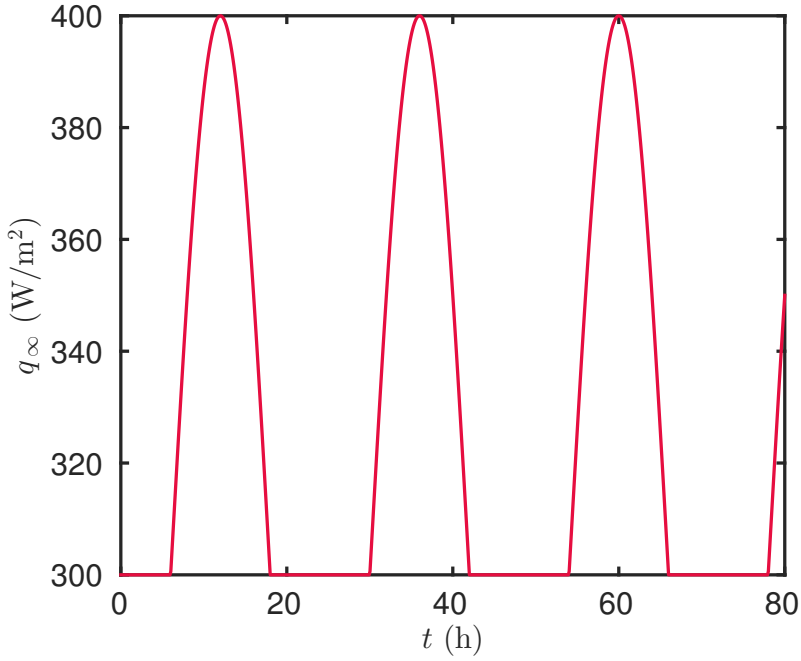

(b)

Figure 17. *Illustration of the case study (a) and outside radiative heat flux (b) for the nonlinear case.*

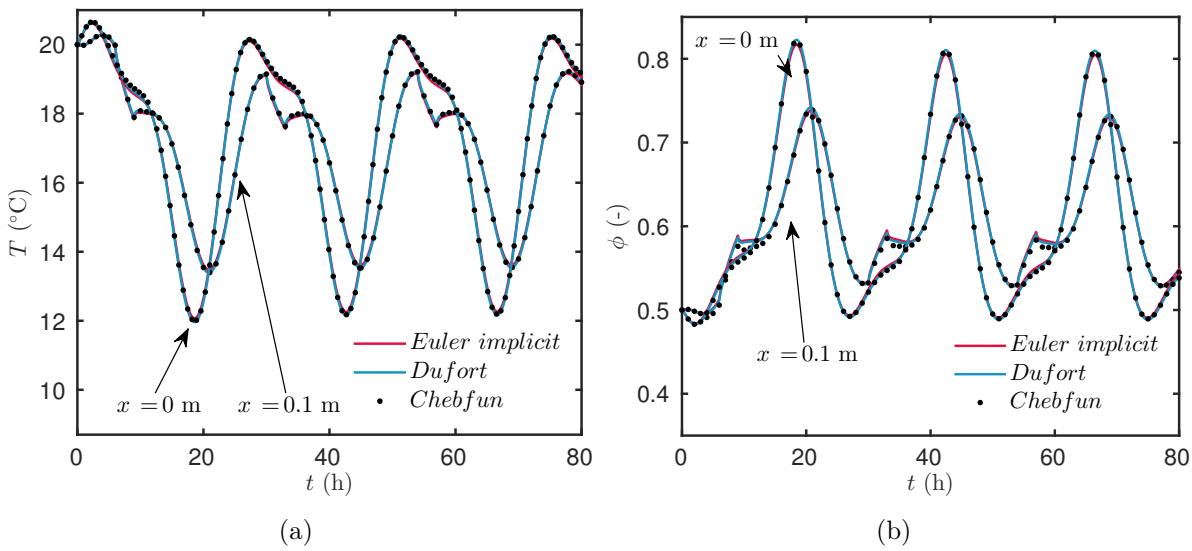

Figure 18. *Evolution of the temperature (a) and relative humidity (b) for the wall* 1 *for the nonlinear case.*

Wall model with nonlinear wall material properties			
Numerical Scheme	CPU time (s)	CPU time (%)	Average number of iterations
explicit Dufort–Frankel	150	28	-
implicit Euler	530	100	3
whole-building model with linear wall material properties			
Numerical Scheme	CPU time (s)	CPU time (%)	Average number of iterations
explicit Dufort–Frankel	8.5	9	-
implicit Euler	95	100	2.95
whole-building model with nonlinear wall material properties			
Numerical Scheme	CPU time (s)	CPU time (%)	Average number of iterations
explicit Dufort–Frankel	480	5.1	-
implicit Euler	8900	100	6

Table 2. *Computer run time required for the numerical schemes.*

package. It also enhanced that the Dufort–Frankel scheme can overcome the disadvantages of the implicit and explicit Euler approaches. First, it is unconditionally stable, enabling to compute the solution for any choice of the time discretisation Δt. The time step is chosen only in accordance with the characteristic time of the physical phenomena

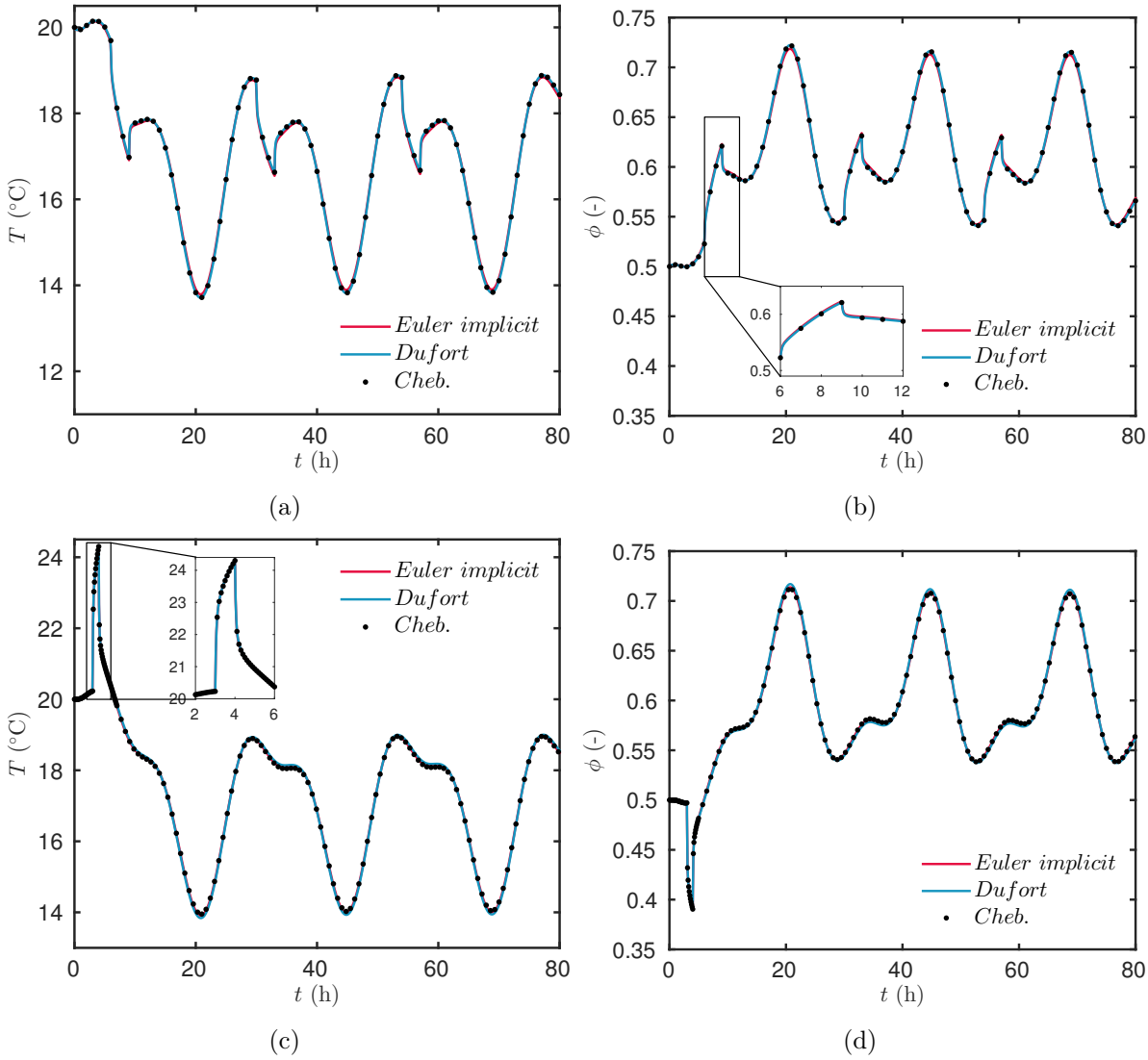

Figure 19. *Evolution of the temperature and relative humidity for zone* 1 *(a-b) and zone* 2 *(c-d) for the nonlinear case.*

[12]. It has also been confirmed that the Dufort–Frankel scheme is second-order accurate in time $\mathcal{O}(\Delta t^2)$ whereas Euler schemes are first-order only. Then, when dealing with nonlinearities, the scheme does not require any sub-iteration at each time step. The solution is directly computed, reducing consequently the computational cost of the algorithm. For the case study considering only heat and moisture transfer through a porous material, the implicit Euler scheme requires around 9 sub-iterations. Therefore the computational cost is reduced by the factor of fifteen using the Dufort–Frankel scheme. When coupling the wall and zone models using implicit schemes, a nonlinear system of equations has to be solved. For the case study, this nonlinearity induces around 3 sub-iterations at each time iteration. When using the explicit Dufort–Frankel scheme, the system

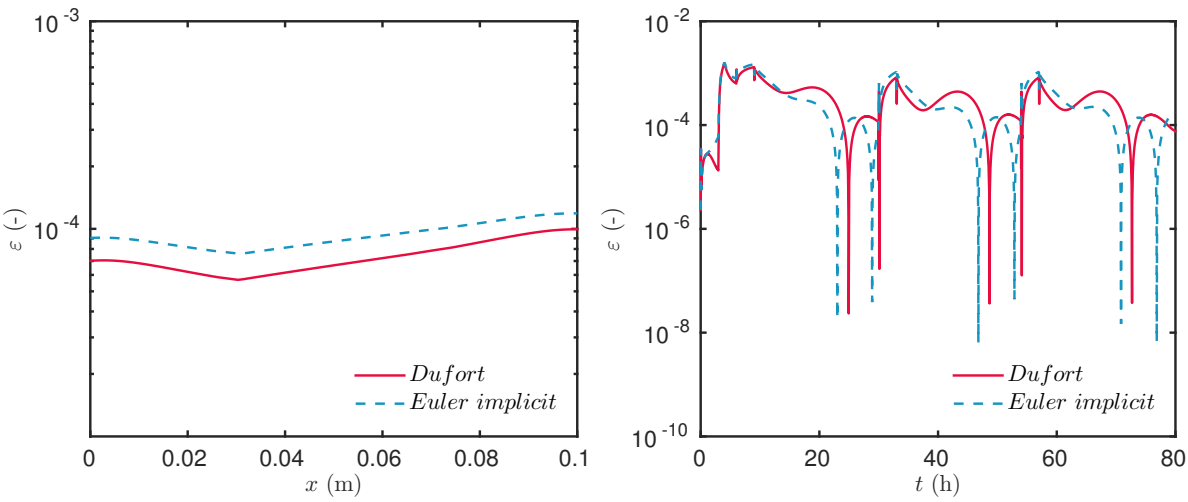

(a) (b)

Figure 20. *Error of the solutions computed with the implicit* Euler *and explicit* Dufort–Frankel *schemes for the walls (a) and for the air zones (b) for the nonlinear case.*

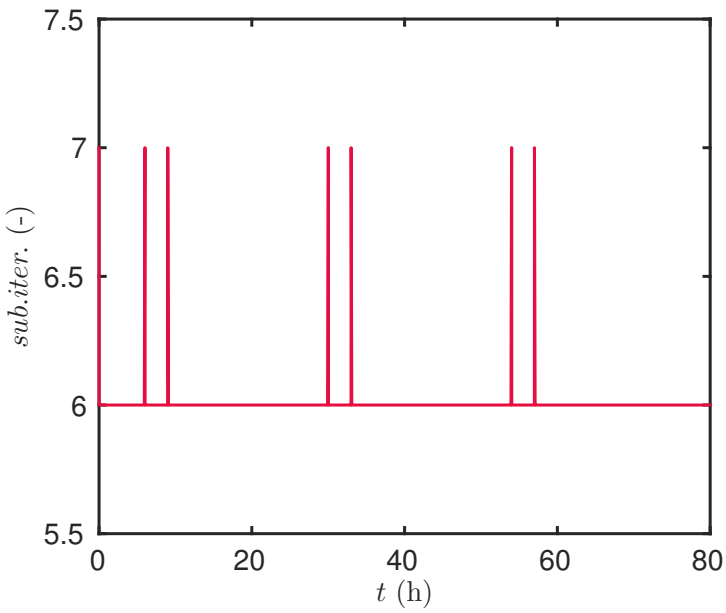

Figure 21. *Sub-iterations required for the implicit* Euler *scheme compute the solution of the whole-building energy model for the nonlinear case.*

of equations becomes linear and no sub-iterations are necessary. Therefore, within the Dufort–Frankel approach, the algorithm requires 9% of the CPU time of the implicit based approach. When considering the nonlinearities of the wall material properties and

long-wave ratiative heat transfer among the room surfaces, the computational savings rise to 95%.

These results are encouraging to apply the Dufort–Frankel approach in building simulation tools. The computational gains should increase with the number of rooms, walls, partitions and furniture. Besides, this improved explicit method can also bring important computational benefits for simulation of building communities, mainly when considering all the interaction among all neighboring outdoor surfaces and elements that affect their energy performance. In addition, this approach is more easily parallelised, achieving almost perfect scaling on high-performance computer systems [7]. To conclude, explicit methods applied to building simulation tools enable perfect synchronism for simulation and co-simulation, which can reduce even more the computation efforts and might be a future trend for complex and accurate energy assessment of a whole-building or even communities of buildings.

Acknowledgements

The authors acknowledge the Brazilian Agencies CAPES of the Ministry of Education and CNPQ of the Ministry of Science, Technology and Innovation, for the financial support.

A. The Dufort–Frankel scheme for weakly coupled equations

This appendix details the application of the Dufort–Frankel approach for two weakly coupled equations, as the ones describing the heat and moisture transfer in porous materials (Section 2). For this purpose, we consider a uniform discretisation as described in Section 3 and the following linear coupled diffusion equation:

$$\frac{\partial v}{\partial t} = \mathrm{Fo}_M \frac{\partial^2 v}{\partial x^2}, \tag{A.1a}$$

$$\frac{\partial u}{\partial t} + \gamma \frac{\partial v}{\partial t} = \mathrm{Fo}_{TT} \frac{\partial^2 u}{\partial x^2} + \gamma \mathrm{Fo}_{TM} \frac{\partial^2 v}{\partial x^2}. \tag{A.1b}$$

The boundary conditions associated to Eq. (A.1) are written as:

$$\frac{\partial v}{\partial x} = \mathrm{Bi}_M \left(v - v_\infty \right), \tag{A.2a}$$

$$\mathrm{Fo}_{TT} \frac{\partial u}{\partial x} + \gamma \mathrm{Fo}_{TM} \frac{\partial v}{\partial x} = \mathrm{Bi}_{TT} \left(u - u_\infty \right) + \mathrm{Bi}_{TM} \left(v - v_\infty \right), \tag{A.2b}$$

Considering Eq. (A.1a) and the straightforward application of the Dufort–Frankel scheme described in Section 3.3, we get:

$$v_j^{n+1} = \frac{1 - \lambda}{1 + \lambda} v_j^{n-1} + \frac{\lambda}{1 + \lambda} \left(v_{j+1}^n + v_{j-1}^n \right), \quad j = 1, \ldots, N, n \geqslant 1, \tag{A.3}$$

where:

$$\lambda \overset{\text{def}}{:=} 2\,\mathrm{Fo}_M \frac{\Delta t}{\Delta x^2}\,.$$

For Eq. (A.1b), the numerical scheme is expressed as:

$$\begin{aligned}\frac{u_j^{n+1} - u_j^{n-1}}{2\,\Delta t} + \gamma \frac{v_j^{n+1} - v_j^{n-1}}{2\,\Delta t} &= \mathrm{Fo}_{TT} \frac{u_{j-1}^n - \left(u_j^{n-1} + u_j^{n+1}\right) + u_{j+1}^n}{\Delta x^2} \\ &\quad + \gamma\,\mathrm{Fo}_{TM} \frac{v_{j-1}^n - \left(v_j^{n-1} + v_j^{n+1}\right) + v_{j+1}^n}{\Delta x^2}\,, \\ j &= 1, \ldots, N\,, n \geqslant 1\,, \end{aligned} \tag{A.4}$$

With Eq. (A.3) and rearranging the terms of Eq. (A.4), the numerical scheme is derived as follows for the field u:

$$\begin{aligned} u_j^{n+1} &= \frac{1 - \mu}{1 + \mu} u_j^{n-1} + \frac{\mu}{1 + \mu}\left(u_{j+1}^n + u_{j-1}^n\right) \\ &\quad + \frac{\gamma - \beta}{1 + \mu} v_j^{n-1} + \frac{\beta}{1 + \mu}\left(v_{j+1}^n + v_{j-1}^n\right) - \frac{\gamma + \beta}{1 + \mu} v_j^{n+1}\,, \quad n \geqslant 1\,, \end{aligned} \tag{A.5}$$

where:

$$\beta \overset{\text{def}}{:=} 2\,\mathrm{Fo}_{TM}\,\gamma \frac{\Delta t}{\Delta x^2} \qquad \text{and} \qquad \mu \overset{\text{def}}{:=} 2\,\mathrm{Fo}_{TT} \frac{\Delta t}{\Delta x^2}\,.$$

For the boundary conditions, the application of the Dufort–Frankel scheme to Eq. (A.2a) gives:

$$\frac{v_2^n - v_0^n}{2\,\Delta x} = \mathrm{Bi}_M \left(\frac{v_1^{n+1} + v_1^{n-1}}{2} - v_\infty \right). \tag{A.6}$$

Here, the node $j = 0$ is a ghost one located a distance Δx from the node $j = 1$. From Eq. (A.6), we can deduce v_0:

$$v_0^n = v_2^n - 2\,\mathrm{Bi}_M\,\Delta x \left(\frac{v_1^{n+1} + v_1^{n-1}}{2} - v_\infty \right). \tag{A.7}$$

In a similar way for Eq. (A.2b), we get:

$$\begin{aligned} u_0^n = u_2^n + \frac{\mathrm{Fo}_{TM}}{\mathrm{Fo}_{TT}}\gamma\left(v_2^n - v_0^n\right) - 2\,\mathrm{Bi}_{TT}\,\Delta x \left(\frac{u_1^{n+1} + u_1^{n-1}}{2} - u_\infty \right) \\ - 2\,\mathrm{Bi}_{TM}\,\Delta x \left(\frac{v_1^{n+1} + v_1^{n-1}}{2} - v_\infty \right). \end{aligned} \tag{A.8}$$

Using Eqs. (A.7) and (A.8), it is possible to compute Eqs. (A.3) and(A.5) for $j = 1$. A similar approach is adopted for node $j = N$.

B. Dimensionless numerical values

This Appendix provides the dimensionless values of the linear case study considered in this work.

B.1. Wall model with linear material properties

In Section 4.1, the dimensionless properties of the material are:

$$\mathrm{Fo}_M = 1.16 \cdot 10^{-2}, \quad \mathrm{Fo}_{TT} = 1.61 \cdot 10^{-1}, \quad \mathrm{Fo}_{TM} = 1.08,, \quad \gamma = 2.35 \cdot 10^{-2},$$

and

$$c_M^\star = k_M^\star = c_{TT}^\star = c_{TM}^\star = k_{TT}^\star = k_{TM}^\star = 1\,.$$

The Biot numbers are $\mathrm{Bi}_M = 3.65$, $\mathrm{Bi}_{TT} = 6.45$ and $\mathrm{Bi}_{TM} = 5.14 \cdot 10^{-1}$ at $x = 0$ and $\mathrm{Bi}_M = 5.48 \cdot 10^{-1}$, $\mathrm{Bi}_{TT} = 2.06$ and $\mathrm{Bi}_{TM} = 7.72 \cdot 10^{-2}$ at $x = 1$, respectively. The boundary conditions are expressed as:

$$\text{At } x = 0, \quad u_\infty = 1 - 0.02 \sin\left(2\pi \frac{t}{60}\right)^2, \quad v_\infty = 1 + 0.3 \sin\left(2\pi \frac{t}{5}\right),$$

$$\text{At } x = 1, \quad u_\infty = 1 + 0.01 \sin\left(2\pi \frac{t}{10}\right), \quad v_\infty = 1 + 0.5 \sin\left(2\pi \frac{t}{8}\right).$$

The final simulation time is fixed to $\tau^\star = 120$.

B.2. Whole-building model with linear material properties

The dimensionless properties of the wall materials, considered in Section 6.1, are:

N. Wall:	$\mathrm{Fo}_M = 1.16 \cdot 10^{-1}$,	$\mathrm{Fo}_{TT} = 1.37 \cdot 10^{-1}$,	$\mathrm{Fo}_{TM} = 3.76$,	$\gamma = 7.87 \cdot 10^{-3}$,
S. Wall:	$\mathrm{Fo}_M = 8.9 \cdot 10^{-2}$,	$\mathrm{Fo}_{TT} = 2.36 \cdot 10^{-1}$,	$\mathrm{Fo}_{TM} = 1.07 \cdot 10^{-1}$,	$\gamma = 3.07 \cdot 10^{-2}$,
E. and W.:	$\mathrm{Fo}_M = 3.23 \cdot 10^{-2}$,	$\mathrm{Fo}_{TT} = 1.61 \cdot 10^{-1}$,	$\mathrm{Fo}_{TM} = 1.08$,	$\gamma = 2.35 \cdot 10^{-2}$,

and for all the walls:

$$c_M^\star = k_M^\star = c_{TT}^\star = c_{TM}^\star = k_{TT}^\star = k_{TM}^\star = 1\,.$$

At $x = 0$, the Biot numbers are:

North Wall:	$\mathrm{Bi}_M = 3.39$,	$\mathrm{Bi}_{TT} = 1.7$,	$\mathrm{Bi}_{TM} = 6.78 \cdot 10^{-1}$,
South Wall:	$\mathrm{Bi}_M = 2.73$,	$\mathrm{Bi}_{TT} = 2.97$,	$\mathrm{Bi}_{TM} = 9.48 \cdot 10^{-1}$,
East and West Walls:	$\mathrm{Bi}_M = 7.31$,	$\mathrm{Bi}_{TT} = 3.1$,	$\mathrm{Bi}_{TM} = 1.03$,

and at $x = 1$

North Wall:	$\mathrm{Bi}_M = 5.09 \cdot 10^{-1}$,	$\mathrm{Bi}_{TT} = 2.72$,	$\mathrm{Bi}_{TM} = 1.01 \cdot 10^{-1}$,
South Wall:	$\mathrm{Bi}_M = 1.02 \cdot 10^{-1}$,	$\mathrm{Bi}_{TT} = 9.5 \cdot 10^{-1}$,	$\mathrm{Bi}_{TM} = 3.55 \cdot 10^{-2}$,
East and West Walls:	$\mathrm{Bi}_M = 5.48 \cdot 10^{-1}$,	$\mathrm{Bi}_{TT} = 2.06$,	$\mathrm{Bi}_{TM} = 7.72 \cdot 10^{-2}$,

For the zone model, the properties are $\kappa_{TT,0} = 1$, $\kappa_{TT,1} = 1.43 \cdot 10^{-2}$ and the coupling parameter θ:

North Wall:	$\theta_T = 3.45$,	$\theta_M = 111.1$,
South Wall:	$\theta_T = 9.89$,	$\theta_M = 55.3$,
East and West Walls:	$\theta_T = 2.27$,	$\theta_M = 5.18$,

The source term due to ventilation system equals:

$$q^\star_{v,1} = 7.1 \cdot 10^{-3}, \qquad q^\star_{v,2} = 3.09 \cdot 10^{-2}, \qquad g^\star_v = 0.5.$$

The source term due to moisture load equals:

$$q^\star_o = 3.8 \cdot 10^{-3} + \begin{cases} 6.1 \cdot 10^{-2}, & t \in [6,9] \\ 6.1 \cdot 10^{-2}, & t \in [6,9] + 24 \\ 6.1 \cdot 10^{-2}, & t \in [6,9] + 48 \\ 0 & \text{otherwise} \end{cases}$$

$$g^\star_o = 6.25 \cdot 10^{-2} + \begin{cases} 1, & t \in [6,9] \\ 1, & t \in [6,9] + 24 \\ 1, & t \in [6,9] + 48 \\ 0 & \text{otherwise} \end{cases}$$

The outside boundary conditions are expressed as:

$$u_\infty = 1 - 0.02 \sin\left(2\pi \frac{t}{24}\right)^2, \qquad v_\infty = 1 + 0.06 \sin\left(2\pi \frac{t}{24}\right).$$

The final simulation time is fixed to $\tau^\star = 80$.

Nomenclature

Latin letters		
A	surface	$[\mathrm{m}^2]$
$c_{p,a}$	air specific heat capacity	$[\mathrm{J/kg.K}]$
$c_{p,v}$	vapour specific heat capacity	$[\mathrm{J/kg.K}]$
c_0	material specific heat capacity	$[\mathrm{J/kg.K}]$
c_w	liquid water specific heat capacity	$[\mathrm{J/kg.K}]$
c_M	moisture storage coefficient	$[\mathrm{s^2/m^2}]$
c_{TM}	coupling storage coefficient	$[\mathrm{W.s^3/kg.m^3}]$
c_{TT}	energy storage coefficient	$[\mathrm{W.s/m^3.K}]$
h_M	convective vapour transfer coefficient	$[\mathrm{s/m}]$
h_T	convective heat transfer coefficient	$[\mathrm{w/m^2.K}]$
g_{inf}	liquid flow	$[\mathrm{kg/m^2.s}]$
g	flow	$[\mathrm{kg/m^2.s}]$
G	room moisture source term	$[\mathrm{kg/s}]$
k_l	liquid permeability	$[\mathrm{kg/m^3/Pa}]$
k_M	moisture transf. coeff. under vap. press. grad.	$[\mathrm{s}]$
k_{TM}	heat transf. coeff. under vap. press. grad.	$[\mathrm{W.s^2/kg}]$
k_{TT}	heat transf. coeff. under temp. grad.	$[\mathrm{W/m.K}]$
L	length	$[\mathrm{m}]$
L_v	latent heat of evaporation	$[\mathrm{J/kg}]$
P_a	air pressure	$[\mathrm{Pa}]$
P_c	capillary pressure	$[\mathrm{Pa}]$
P_s	saturation pressure	$[\mathrm{Pa}]$
P_v	vapour pressure	$[\mathrm{Pa}]$
Q	room heat source term	$[\mathrm{W/m^3}]$
q	heat flux	$[\mathrm{W/m^2}]$
R_v	water gas constant	$[\mathrm{J/kg.K}]$
T	temperature	$[\mathrm{K}]$
s	view factor	$[-]$
V	volume	$[\mathrm{m^3}]$
w_a	humidity ratio	$[\mathrm{kg/kg}]$

Greek letters		
δ_v	permeability	[s]
σ	STEFAN–BOLTZMANN constant	[−]
ϕ	relative humidity	[−]
ρ	specific mass	[kg/m^3]

Parameters involved in the dimensionless representation		
Bi	BIOT number	[−]
c, κ	storage coefficient	[−]
Fo	FOURIER number	[−]
k	permeability coefficient	[−]
q, g	source terms	[−]
u, u_a, v, v_a	field	[−]
θ	weighted contribution	[−]
ν	diffusion coefficient	[−]

References

[1] R. M. Barbosa and N. Mendes. Combined simulation of central HVAC systems with a whole-building hygrothermal model. *Energy and Buildings*, 40(3):276–288, jan 2008. 31

[2] B. Bauklimatik Dresden. Simulation program for the calculation of coupled heat, moisture, air, pollutant, and salt transport. *http://www.bauklimatik-dresden.de/delphin/index.php?aLa=en*, 2011. 4

[3] J. Berger, S. Guernouti, M. Woloszyn, and F. Chinesta. Proper Generalised Decomposition for heat and moisture multizone modelling. *Energy and Buildings*, 105:334–351, 2015. 18

[4] J. Berger, W. Mazuroski, N. Mendes, S. Guernouti, and M. Woloszyn. 2D whole-building hygrothermal simulation analysis based on a PGD reduced order model. *Energy and Buildings*, 112:49–61, jan 2016. 18

[5] D. M. Burch. An Analysis of Moisture Accumulation in Walls Subjected to Hot and Humid Climates. *ASHRAE Transactions*, 93(16):429–439, 1993. 4, 23

[6] E. Cajori. Historical note on the Newton-Raphson method ofapproximation. *Amer. Math.*, 18:29–32, 1911. 10

[7] B. N. Chetverushkin and A. V. Gulin. Explicit schemes and numerical simulation using ultrahigh-performance computer systems. *Doklady Mathematics*, 86(2):681–683, sep 2012. 36

[8] G. H. dos Santos and N. Mendes. Analysis of numerical methods and simulation time step effects on the prediction of building thermal performance. *Applied Thermal Engineering*, 24(8-9):1129–1142, jun 2004. 23

[9] G. H. Dos Santos and N. Mendes. Simultaneous heat and moisture transfer in soils combined with building simulation. *Energy and Buildings*, 38(4):303–314, 2006. 4, 20

[10] T. A. Driscoll, N. Hale, and L. N. Trefethen. Chebfun Guide. *Pafnuty Publications*, Oxford, 2014. 12

[11] I. Fraunhofer. Wufi. *http://www.hoki.ibp.fhg.de/wufi/wufi_frame_e.html*, 2005. 4

[12] S. Gasparin, J. Berger, D. Dutykh, and N. Mendes. Stable explicit schemes for simulation of nonlinear moisture transfer in porous materials. *J. Building Perf. Simul.*, pages 1–21, 2017. 4, 11, 14, 24, 34

[13] C.-E. Hagentoft, A. S. Kalagasidis, B. Adl-Zarrabi, S. Roels, J. Carmeliet, H. Hens, J. Grunewald, M. Funk, R. Becker, D. Shamir, O. Adan, H. Brocken, K. Kumaran, and R. Djebbar. Assessment Method of Numerical Prediction Models for Combined Heat, Air and Moisture Transfer in Building Components: Benchmarks for One-dimensional Cases. *J. Building Phys.*, 27(4):327–352, apr 2004. 13, 14

[14] J. L. M. Hensen. Modelling coupled heat and air flow: ping-pong vs onions. In *IEA Air infiltration and Ventilation Centre Coventry UK Conference*, pages 253–262, 1995. 4

[15] H. Janssen. Simulation efficiency and accuracy of different moisture transfer potentials. *Journal of Building Performance Simulation*, 7(5):379–389, sep 2014. 4, 5, 13, 14

[16] H. Janssen, B. Blocken, and J. Carmeliet. Conservative modelling of the moisture and heat transfer in building components under atmospheric excitation. *Int. J. Heat Mass Transfer*, 50(5-6):1128–1140, mar 2007. 4

[17] W. Kahan and J. Palmer. On a proposed floating-point standard. *ACM SIGNUM Newsletter*, 14(si-2):13–21, oct 1979. 7

[18] A. S. Kalagasidis, P. Weitzmann, T. R. Nielsen, R. Peuhkuri, C.-E. Hagentoft, and C. Rode. The International Building Physics Toolbox in Simulink. *Energy and Buildings*, 39(6):665–674, jun 2007. 4

[19] N. Mendes. *Models for prediction of heat and moisture transfer through porous building elements*. PhD thesis, Federal University of Santa Catarina - UFSC, 1997. 4, 23

[20] N. Mendes and P. C. Philippi. A method for predicting heat and moisture transfer through multilayered walls based on temperature and moisture content gradients. *Int. J. Heat Mass Transfer*, 48(1):37–51, 2005. 4

[21] N. Mendes, I. Ridley, R. Lamberts, P. C. Philippi, and K. Budag. Umidus: A PC program for the Prediction of Heat and Mass Transfer in Porous Building Elements. In *IBPSA 99*, pages 277–283, Japan, 1999. International Conference on Building Performance Simulation. 4, 23

[22] A. Nayfeh. *Perturbation Methods*. Wiley-VCH, New York, 1 edition, 2000. 7

[23] J. Raphson. Analysis aequationum universalis seu adaequationes algebraicas resolvendas methodus generalis, et expedita, ex nova infinitarum serierum doctrina deducta ac demonstrata. *Microfilm copy: University Microfilms*, Ann Arbor(MI), 1690. 10

[24] R. D. Richtmyer and K. W. Morton. *Difference Methods for Initial-Value Problems*. Interscience Publishers, New York, 1967. 11

[25] C. Rode and K. Grau. Whole Building Hygrothermal Simulation Model. *ASHRAE Transactions*, 109(1):572–582, 2003. 4, 23

[26] S. Rouchier, M. Woloszyn, G. Foray, and J.-J. Roux. Influence of concrete fracture on the rain infiltration and thermal performance of building facades. *Int. J. Heat Mass Transfer*, 61:340–352, jun 2013. 4, 5

[27] H.-J. Steeman, M. Van Belleghem, A. Janssens, and M. De Paepe. Coupled simulation of heat and moisture transport in air and porous materials for the assessment of moisture related damage. *Building and Environment*, 44(10):2176–2184, oct 2009. 4

[28] F. Tariku, K. Kumaran, and P. Fazio. Transient model for coupled heat, air and moisture transfer through multilayered porous media. *Int. J. Heat Mass Transfer*, 53(15-16):3035–3044, jul 2010. 5, 18

[29] P. J. Taylor. The stability of the Du Fort-Frankel method for the diffusion equation with boundary conditions involving space derivatives. *The Computer Journal*, 13(1):92–97, jan 1970. 11

[30] M. T. van Genuchten. A comparison of numerical solutions of the one-dimensional unsaturated - saturated flow and mass transport equations. *Adv. in Water Ressources*, 5(1):47–55, mar 1982. 4

[31] M. Woloszyn and C. Rode. Tools for performance simulation of heat, air and moisture conditions of whole buildings. *Building Simulation*, 1(1):5–24, mar 2008. 4

S. Gasparin: Thermal Systems Laboratory, Mechanical Engineering Graduate Program, Pontifical Catholic University of Paraná, Rua Imaculada Conceição, 1155, CEP: 80215-901, Curitiba – Paraná, Brazil
E-mail address: suelengasparin@hotmail.com
URL: https://www.researchgate.net/profile/Suelen_Gasparin/

J. Berger: Thermal Systems Laboratory, Mechanical Engineering Graduate Program, Pontifical Catholic University of Paraná, Rua Imaculada Conceição, 1155, CEP: 80215-901, Curitiba – Paraná, Brazil
E-mail address: Julien.Berger@pucpr.edu.br
URL: https://www.researchgate.net/profile/Julien_Berger3/

D. Dutykh: LAMA, UMR 5127 CNRS, Université Savoie Mont Blanc, Campus Scientifique, F-73376 Le Bourget-du-Lac Cedex, France
E-mail address: Denys.Dutykh@univ-savoie.fr
URL: http://www.denys-dutykh.com/

N. Mendes: Thermal Systems Laboratory, Mechanical Engineering Graduate Program, Pontifical Catholic University of Paraná, Rua Imaculada Conceição, 1155, CEP: 80215-901, Curitiba – Paraná, Brazil
E-mail address: Nathan.Mendes@pucpr.edu.br
URL: https://www.researchgate.net/profile/Nathan_Mendes/